Design and Characterization of Probe and Control laser system for experiment with ultracold Ytterbium Rydberg atoms

Master Thesis

Written by	Aksel Vendelsøe Nielsen
Email	aknie14@student.sdu.dk
Supervisor	Prof. Sebastian Hofferberth
Delivery date	1/6-19

University of Southern Denmark,
Department of Physics, Chemistry and Pharmacy

Abstract

This thesis reports on developing a new nonlinear quantum optics experiment for studying ultra-cold ytterbium Rydberg atoms. The experiment aims for using the advantages of ytterbium to create a large, free-space medium in which which many-body phenomena of strongly interacting Rydberg-polaritons can be investigated.

The field of non-linear quantum optics concerns itself with creating and investigating optical systems in which individual photons interact strongly. The ultimate goal of this research area is investigation into exotic quantum many-body states of light such as photon liquids and photon crystals, quantum computation and quantum simulation. This would offer new insight into the elementary basis of quantum physics, and furthermore opens up for technological advances in high-speed information processing.

This thesis primarily concerns itself with the designing and characterization of the probe and control laser setup.

Resumé

I dette special beskrives designet og inplementeringen af en ny eksperimentel opstilling som skal bruges til eksperimenter med Rydbergatommedieret ulineær kvanteoptik med det jordal-kalimetallignende grundstof ytterbium.

Feltet for ikke-lineær kvanteoptik beskæftiger sig med at skabe og undersøge optiske systemer. Det ultimative mål for dette forskningsområde er forskning i kvanteberegning og kvantsimulering. Dette vil give en ny indsigt i det grundliggende grundlag for kvantefysik, og åbner desuden for teknologiske fremskridt inden for højhastighedsinformationsbehandling.

Denne afhandling beskæftiger sig primært med design og karakterisering af probe- og kontrol-laseropsætningen.

Contents

Introduction

The field of non-linear quantum optics concerns itself with creating and investigating optical systems in which individual photons interact strongly. The ultimate goal of this research area is investigation into exotic quantum many-body states of light such as photon liquids and photon crystals [1–4], quantum computation [5] and quantum simulation [6]. This would offer new insight into the elementary basis of quantum physics, and furthermore opens up for technological advances in high-speed information processing [7].

As the photon-photon scattering cross-section is nearly non-existent in free space, atom-photon interaction are used instead. The coupling of the light-field to a single atom is also very weak, as a consequence of low optical nonlinearities. This results nonlinear effects, like spontaneous parametric up/down conversion, only occurs at high intensities [8]. By confining light temporally and spatially in a cavity [9] or in a waveguide [10], this non-linearity can be increased. Another approach is to exploit the long-range, dipole-dipole interactions of Rydberg atoms [11, 12], combined with electromagnetically induced transparency (EIT). This method can create effective interaction between individual photons [13]. Ryberg atoms have extreme properties in terms of the size, polarizability, lifetime and have strong interaction with other atoms, which is tunable from van-der-Waals to dipole-dipole interaction [14]. Utilizing the strong atom-atom interactions, the excitation of a second nearby atom to the Rydberg state is suppressed. This phenomenon is called the Rydberg blockade mechanism, and is caused by an energy shift of the Rydberg levels of the nearby atoms [15]. Due to the blockade effect nonlinearities can be realized at a single photon level. By use of the Rydberg blockade mechanism, entanglement of an entire ensemble of atoms and coherent manipulation by a single photon can be realized [16, 17]. In the EIT process the optical phenomenon that an opaque medium can be rendered transparent by means of destructive interference of the quantum mechanical transition amplitudes of a two-photon transition [18]. As a photon enters a medium with induced transparency conditions, it gets excited to a quasi-particle, termed dark-state polariton [19], which features a number of interesting properties, such as a group velocity more than a million times slower than the speed of light in vacuum [20].

The combination of these two techniques maps the interaction of the Rydberg atoms onto the ongoing photons. A Rydberg-polariton propagates slowly through the medium and suppresses any further excitation of Rydberg atoms, by means of the Rydberg blockade mechanism. This behaviour can induce changes of the photon characteristics of transmitted light between classical and non-classical behaviour. Proposed in 2005 [13] this new way of manipulating single photons and generating non-classical light were for the first time realized in 2010 [21]. Since then the field of Rydberg atoms has advanced considerably. Likewise, the theoretical framework of the underlying mechanisms of Rydberg atoms was expanded during this time

[1, 2, 22–24].

As alkali atoms have a simple electron structure, akin to the hydrogen atom, almost all Rydberg atom experiments during the last 10 years have used them. Lately, a noticeable trend towards the use of alkaline-earth-like atoms in Rydberg experiments can be seen [25–29]. As the alkaline-earth-like atoms have a more complex electron structure than alkali, they may pave the way for discovering new Rydberg physics phenomena. The most obvious difference compared to alkali atoms is the presence of two valence electrons. This allows for the production of both singlet and triplet states, which exhibits a diversity of attractive and repulsive interactions. Another benefit of an extra valence electron is the possibility of only exciting one valance electron to the Rydberg state, giving an optical active core ion which can be manipulated with a suitable laser [30]. Exciting the second valence electron into low orbital momentum quantum number states leads to autoionization, caused by single violent electron-electron collisions [31]. If the second valence electron is excited to a high orbital quantum number state, no autoionization occurs, allowing for instance optical imaging of the Rydberg states. The second valence electron also makes simultaneously trapping both the ground and Rydberg state possible [32].

Outline of Thesis

This thesis reports on developing a new nonlinear quantum optics experiment for studying ultra-cold ytterbium Rydberg atoms. The experiment aims for using the advantages of ytterbium to create a large, free-space medium in which which many-body phenomena of strongly interacting Rydberg-polaritons can be investigated.

Project was began in February 2018. In the first half of 2018, the location for the new experiment was under construction, and the time was spent by laying out the plan for the final experiment. In the end of the summer, the location was ready and the optical tables were moved in. The work now started on putting all the necessary pieces on the laser table. I joined in September 2018 to a laboratory with most of the experiment under construction. Besides helping with general lab construction, I was assigned the probe and control as my primary focus. In the start of 2019 the experimental chambers were finished and under high vacuum.

The now assembled, but not yet functioning, experiment consist of two vacuum chambers. One chamber will consist of a two-dimensional magneto-optical trap (2D MOT) as a source of cold ytterbium atoms, loaded for a stream of atoms emitted from dispensers. After loading the 2D MOT the atoms will be transferred to another chamber. This ultra-high vacuum chamber is called the science chamber, and consists of a 3D MOT, an optical dipole trap, a electric field control and lasers for exciting the atoms to the Rydberg state.

This thesis is structured as follows. Chapter 1 lays out the theoretical framework necessary to understand the experimental results obtained during the thesis. Chapter 2 gives an overview of the current state of the experiment. Chapter 3 will describe to probe/control setup, and present fiber coupling and polarization stability results. Chapter 4 will lay out all measurements of the spot size of the probe setup, and discuss the polarization issues that was discovered in the end of this thesis. Finally chapter 5 summarizes the obtained results, giving a survey of the current status of the experiment and the immediate outlook and prospects towards exploring Rydberg physics with ultra-cold ytterbium atoms.

1 Theoretical background

This chapter will lay out the necessary theoretical framework for understanding working principles of experiment, especially the design and characterization of the probe and control light, used in the experiment for exciting atoms to the Rydberg state. The first part of this chapter will introduce non-linear quantum optics as a research area and gives the theoretical framework on which this experiment have been designed. Second part of this chapter will explain laser cooling as a method of obtaining ultracold atoms, and motivate ytterbium as a prime candidate as an atomic species well suited for Rydberg physics. The third and final part of this chapter goes in depth with the relevant theory for optics, on which all of the experimental work done during this thesis rest.

1.1 Non-Linear Quantum Optics with Rydberg atoms

During the last two decades controlling quantum effect have been proposed as a key concept for future technology, such as quantum computation and communication. Photons have been identified as ideal carriers of long-distance quantum information.

However, to make this possible, it is necessary to figure out how to manipulate with single photons. This requires nonlinear processes on single photon level [33]. Since nonlinear processes in nature scale with intensity squared (or higher) there needs to be very strong nonlinearity present to be seen a single photon level. To get very strong interaction an enhanced light-matter coupling is required.

This can be done in different ways, either by modifying he light or the optical medium. In high finesse cavities each photon is allowed to interact multiple times with the medium. By using a waveguide it is possible to favour specific modes of the light and thereby prompt the medium to emit primarily into these modes. One can also use a medium which in istelf has a very strong nonlinear response, which can be achieved by using Rydberg atoms.

In the latter approach the photons are mapped onto strongly interacting atomic states, which are then turned back into nonclassical states of light.

Currently, only high finesse cavities and Rydberg systems have gone to single photon non-linearities [34–36].

This thesis has been done with an experiment that is planned to use Rydberg atoms to make nonlinear quantum optics.

Rydberg physics

Rydberg atoms are atoms where a single valence electron has been excited to a highlying state [37]. Compared to ground state atoms, Rydberg atoms have relatively extreme properties, such as size, lifetime, polarizability and so on. These properties scale with principal quantum number n and make Rydberg atoms ideal for nonlinear quantum optics applications [36].

The size scales with n^2, which means that Rydber atoms of 10's of micrometers can be realized. Contraintuitively, due to the vanishing overlap between the ground state and the excited state, the lifetime scales with n^3. The polarizability of Rydberg atoms scales with n^7, and the dipole moment scales with n^2 [37]. Due to these scalings, Rydberg atoms are extremely sensitive to external fields and also to other atoms, especially other Rydberg atoms due to the large induced dipole moments. This gives rise to the so called Rydberg blockade.

For s-states, at large distances, the interaction between Rydberg atoms is Van der Waals type. This means that two Rydberg atoms will repell each other if they are moved together, and that it requires energy to bring them close. Correspondingly, the energy required to make an excitation of an atom to a Rydberg state is dependent on whether the atom is close to other Rydberg atoms.

Thus, for a laser with a given linewidth, it will not be possible to excite atoms within a certain distance from an excisting Rydberg atom to that same Rydberg state. This distance is the blockade radius and depends on the van der Waals coefficient, c_6, and the Rabi frequency of the field driving that transition:

$$r_b = \sqrt[6]{\frac{c_6}{\hbar\Omega}} \tag{1.1}$$

The blockade effect allows for large atomic ensembles to behave collectively. When atoms are collectively excited, they can have enhanced interaction with the driving field, and this is key to strong coupling to even a field with few photons [38].

A collective state of N atoms will however not stay in a collective superposition forever. It loses coherence due to the motion of the individual atoms and due to coupling to light fields.

If we want to excite to a highlying s-state from the ground state in ytterbium, which is also an s-state, it is necessary to go through an intermediate state, as the direct s-s-transition is dipole forbidden. If this excitation is done with two light fields which are counter-propagating, the collective state can be written as a state $|R\rangle$:

$$|R\rangle = \frac{1}{\sqrt{N}} \sum_{j=1}^{N} e^{i(k_c - k_p)r_j} |g_1,...,r_j,...,g_N\rangle \tag{1.2}$$

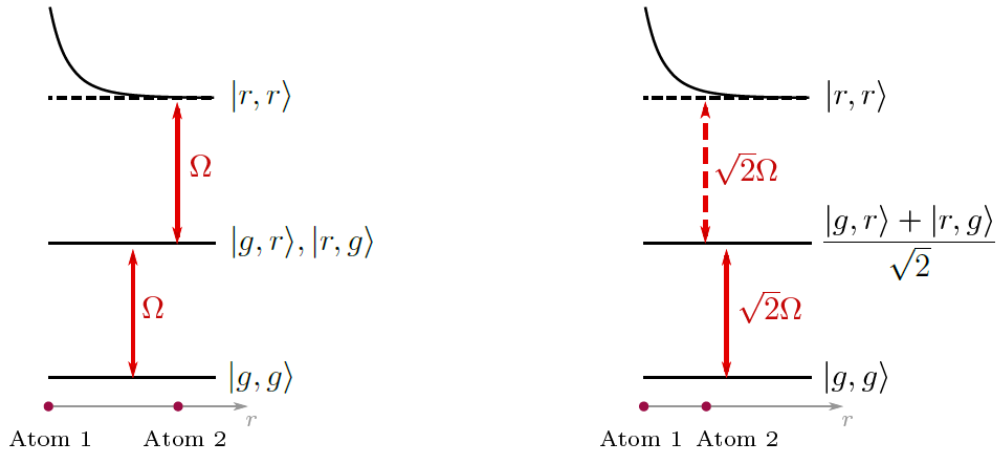Where k_c and k_p are wavevectors of the two driving fields and r_j is the position of the jth

Figure 1: Rydberg level scheme. **Left**: excitation of two Rydberg atoms is allowed if the distance between them is sufficiently large. **Right**: Within the blockade radius, the energy of a second Rydberg excitation is shifted out of resonance. Figure from [39].

atom. The state $|g_1,...,r_j,...,g_N\rangle$ corresponds to the j'th atom being excited to the Rydberg state and all the others being in the ground state [40].

The phasefactor can be rewritten to give the coherence time scale:

$$(k_c - k_p)r_j = 2\pi \left(\frac{1}{\lambda_c} - \frac{1}{\lambda_p} \right) vt := \frac{t}{\tau_{\text{coh}}} \tag{1.3}$$

Here λ_c and λ_p are wavelengths of the two fields and v is the mean velocity of the atoms.

Rydberg atoms have already been applied to realize highly nonclassical states of light [41–43] and a large variety of tools for single photon operations, such as photon sources, gates, single photon absorbers and even single photon transistors [44–48].

Yet many of these tools are limited by decoherence, and this is one of the reasons why the ytterbium experiment is being designed for further experiments with nonlinear quantum optics in Rydberg atoms.

1.2   Ytterbium for Rydberg Physics

Amongst all of the alkaline-earth-like elements, ytterbium (Yb) stands out with a broad range of useful properties that are now used across a number of applications. Early work was done by the group of Y. Takahashi in Kyoto, who were the first to observe degenerate Bose and Fermi gases of Yb [49, 50]. Since then Yb have been used in the investigation of many-body physics in optical lattices for quantum computation [51–55], even with subwavelength spatial structure [56], and in realizing a Mott insulator [57]. The narrow clock-transition of Yb is another interesting property, which allow for the construction of extremely precise atomic clocks [58]. Also transportable atomic clocks for testing gravitational theory are based on Yb [59].

For Rydberg physics, ytterbium also have high potential. The two valence electrons present in all alkaline-earth-like atoms, allows for the possibility of both singlet and triplet Rydberg states [60]. Yb property of both having broad and narrow transitions benefits laser cooling [61] and applications for Rydberg dressing [25]. As wavelength matching of the two-photon transition from ground to Rydberg state minimizes dephasing processes [62]. Yb also has the useful feature that it has a large number of stable isotopes. These isotopes, together with some of their properties can be seen in table 1.

Isotopes	Mass [U]	Abundance %	Nuclear Spin	Statistical behavior
^{168}Yb	167.933 897	0.12	0	bosonic
^{170}Yb	169.934 761 8	2.98	0	bosonic
^{171}Yb	170.936 325 8	14.09	1/2	fermionic
^{172}Yb	171.936 381 5	21.68	0	bosonic
^{173}Yb	172.938 210 8	26.10	5/2	fermionic
^{174}Yb	173.938 862 1	32.03	0	bosonic
^{176}Yb	175.942 571 7	13.00	0	bosonic

Table 1: The seven stable isotopes of Ytterbium. Masses from [63]. Abundance from [64].

Ytterbium is a rare-earth element of the lanthanide series with proton number Z = 70. Its melting point is at 824 ℃ and boiling point at 1196 ℃ [65]. Usually a sufficient ytterbium flux for use in cold atom experiments requires an atomic source to be heated to temperatures between 400 ℃ and 500 ℃. Ytterbium also has a relative low vapour pressure at room temperature of around $p_{\mathrm{Yb,RT}} \approx 10^{-21}$ mbar compared to rubidium, a commonly used element for cold atom experiments, at $p_{\mathrm{Rb,RT}} \approx 10^{-7}$ mbar. Because of the low vapour pressure Yb atoms tend to stick to surfaces it collides with, and several groups have reported problems with Yb coating viewports and blocking for optical access [66, 67].

The electronic structure of Yb is $[\text{Xe}]4f^{14}6s^2$ and resembles the alkaline-earth atoms due to the presence of two valence electrons. On figure 3 the relevant states and transitions for cooling of ^{174}Yb is shown. Each level is denoted with $^{2S+1}L_J$, where S is the total spin, L the total orbital angular momentum and $J = L + S$ the total angular momentum [68].

To excite ytterbium from ground state to a Rydberg state multiple approaches can be taken. Both single- and multi-photon transitions are available. A single photon transition requires ultraviolet light to reach the ionization limit $I_{6S} = 50433.07041 \text{cm}^{-1}$ [68], which is difficult to realize experimentally, as the production of ultraviolet light is hard. A two-photon transition via an intermediate level are instead chosen for exciting Rydberg states, illustrated in figure 2. Both wavelengths are in the optical spectrum and any Doppler-shift can be nullified by counterpropagating the beams. The two-photon transition allows allows for control of the weak probe beam via the EIT mechanism.
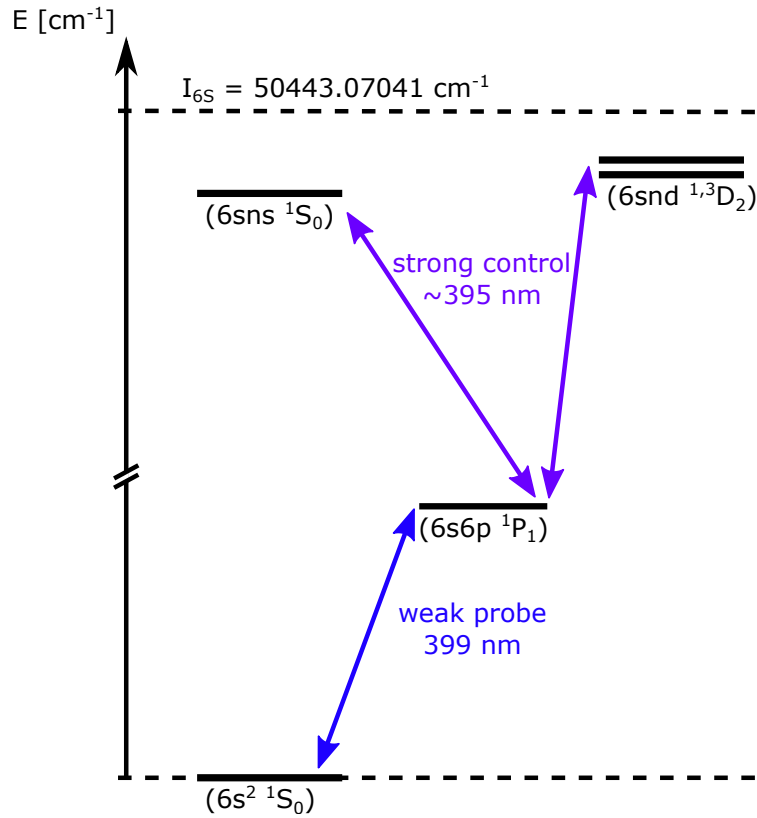

Figure 2: Two-photon transition from ground to Rydberg state. A single photon probe laser is used to couple to an intermediate state, and a strong control laser couples the intermediate state to the Rydberg state.

To summarize, ytterbium has multiple benefits for nonlinear quantum optics experiments when compared to alkali elements. A simple energy level structure with no hyperfine structure and ground states being insensitive to magnetic field due to the vanishing total angular mo-

mentum and nuclear spin. The level scheme also conveniently offers two almost closed-cycle cooling transitions: The dipole allowed $^1S_0 \rightarrow {}^1P_1$ singlet transition and the semi-forbidden triplet transition $^1S_0 \rightarrow {}^3P_1$. The singlet transition can be used for magneto-optical trapping a large amount of atoms [69], while the triplet transition can be used to achieve Doppler temperatures below 40 µK [49].

As described in chapter 1.1 a short wavelength of the probe light is beneficial for extending the Rayleigh length. As Yb can be cooled down to around 10 µK, a longer coherence time can be achieved compared to alkali elements. The presence of fermionic isotopes opens up a new line of research of Rydberg-EIT with fermionic atom species.

For a more in depth description of Yb properties can be found in the following PhD theses [52, 66, 70].
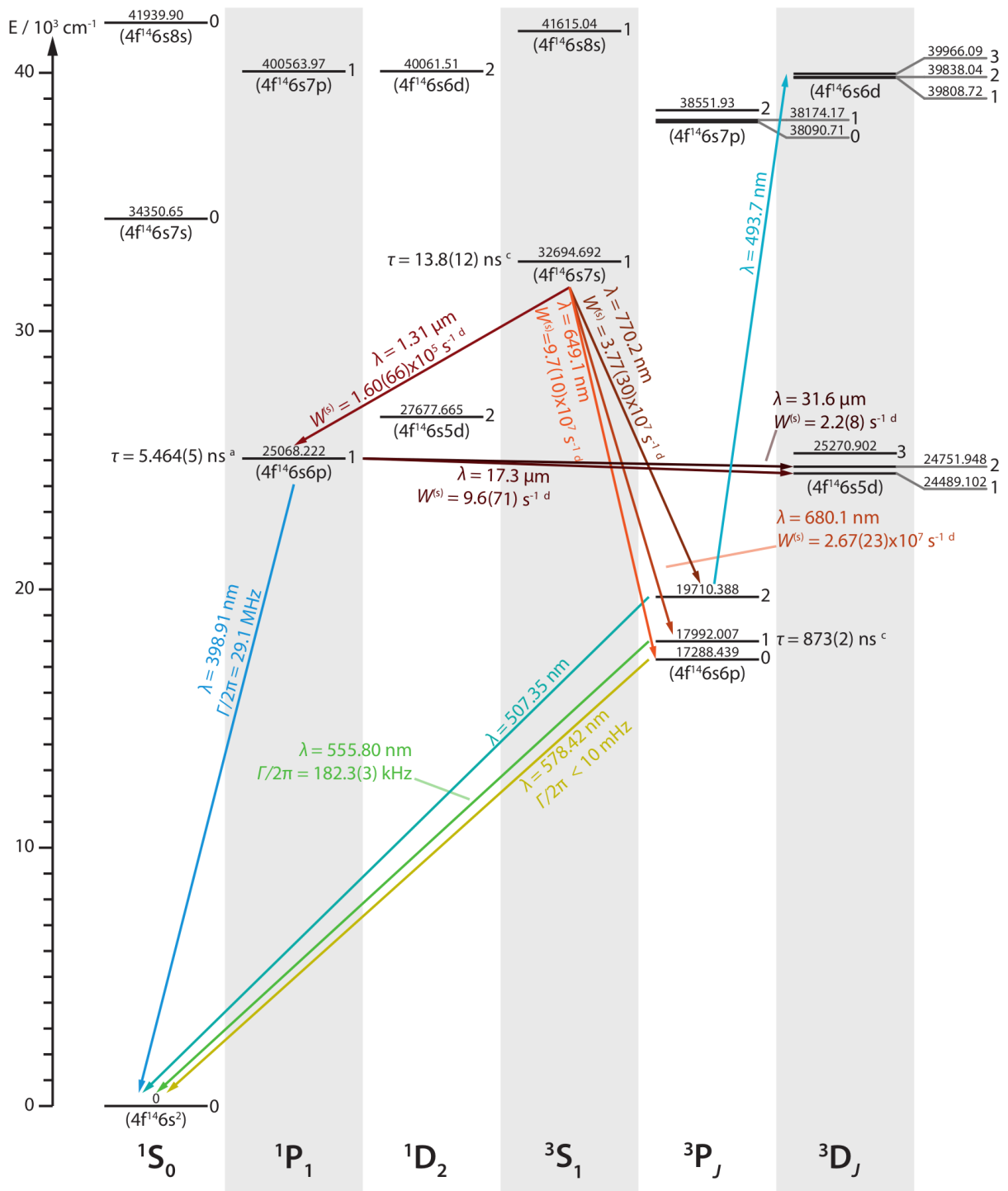
Figure 3: Level diagram for ^{174}Yb with the most relevant levels and transitions for cooling shown. Taken from [66].

1.3 Laser cooling

To realize Rydberg physics, a very important prerequisite is a system with very low temperature, to minimize the loss of coherence caused by thermal motion of the atoms. Another requirement is the ability to spatially confined atoms to increase the light-matter overlap, resulting in stronger interactions. The planned experiment incorporate both a 2-dimensional and a 3-dimensional magneto-optical trap (MOT) for cooling Yb atoms, which will will then be transferred to a dipole trap.

The mechanisms of laser cooling and optical trapping follows from the laws of energy and momentum conversation in an atom-light interaction. Two kinds of radiative forces are important for cooling and trapping. The first is the radiative pressure force, describing the forces an atom experiences, when it absorbs and remits a photon. The second force is the optical dipole force, which stems from the interaction between the electric field and the induced atomic dipole. In this kind of interaction no photon absorption takes place, meaning the frequency of the used light can be far-detuned from the resonance frequency of the atom. In the current experiment, optical dipole trapping is not yet implemented.

The radiation pressure force experienced in the time interval Δt by N_{ph} amount of photons is:

$$\mathbf{F} = \hbar\mathbf{k}\frac{N_{ph}}{\Delta t} \tag{1.4}$$

where $\hbar\mathbf{k}$ is the momentum transferred from each photon to the atom. In [71] equation 1.4 is evaluated assuming that the interaction is between a classical coherent radiant light field and a two-level quantum system. Demonstratively, the radiation pressure force an atom experiences is:

$$\mathbf{F} = \hbar\mathbf{k}\frac{\gamma}{2}\frac{\dfrac{I}{I_{sat}}}{1 + \dfrac{I}{I_{sat}} + \dfrac{4\delta^2}{\gamma^2}} \tag{1.5}$$

Where the atomic saturation intensity is given by

$$I_{sat} = \frac{\hbar\omega^3\gamma}{12\pi c^2} \tag{1.6}$$

and γ is the natural linewidth of the transition, I is the intensity of the laser, and $\delta = \omega - \omega_0$ is the detuning, with ω being the laser frequency and ω_0 the atomic resonance frequency. From equation (1.5) the radiation pressure force has the same direction as the absorbed photon. The radiation pressure scales as I/δ^2 for out-of-resonance frequencies. With zero detuning and at intensities much higher than the saturation intensity, the force goes to $\mathbf{F} = \hbar\mathbf{k}\gamma/2$. When the intensity exceeds the saturation intensity the atoms will be absorbing and re-emitting photons at a rate of $\gamma/2$, which is given by the lifetime of the excited state $\tau = 1/\gamma$.
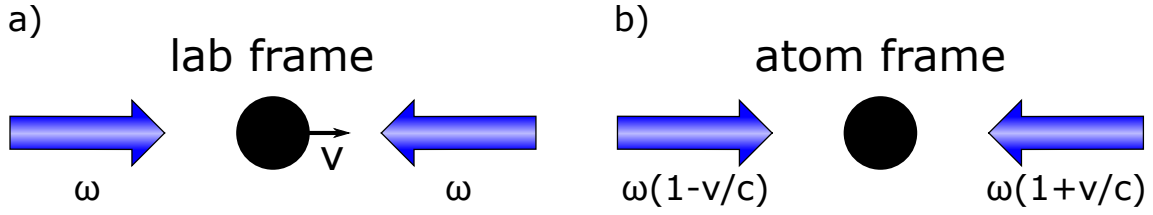
Figure 4: Concept of optical molasses.

To apply the principle of radiative pressure force in a practical way, Jean Dalibard conceived the idea of combining optical molasses with a magnetic gradient, to create the magneto-optical trap (MOT). Optical molasses is made by using two counterpropagating laser beams with frequency ω smaller than the resonance frequency of the atom. Because of the Doppler effect, the atom moving with velocity with modulus v, will see the photons moving the same direction as the atom as being redshifted by $\omega' = \omega(1 - v/c)$, and likewise the photons moving the opposite direction of the atom as being blueshifted $\omega'' = \omega(1 + v/c)$. This is illustrated on figure 4. Since the resonance frequency of the atom is lower than the frequency of the light, the probability of the atom absorbing the upshifted light is more likely. Hence the net result will be a reduction of velocity of the atom. In the low intensity limit, the total force exerted on the atom is described by equation (1.5) where the Doppler shift is included:

$$\mathbf{F} = \hbar\mathbf{k}\frac{\gamma}{2}\left[\frac{\frac{I}{I_{sat}}}{1 + \frac{4(\omega - \omega_0 - kv)^2}{\gamma^2}} - \frac{\frac{I}{I_{sat}}}{1 + \frac{4(\omega - \omega_0 + kv)^2}{\gamma^2}}\right] \tag{1.7}$$

The first term of equation (1.8) is the force from the co-propagating beam, and the second term is the force from the counter-propagating beam. While the optical molasses only cool the atoms, they will still over time end up outside of the cooling area, due the random motion.

To spatially confine the atoms an inhomogeneous magnetic field with a well defined trap center is introduced. Consider a one-dimensional two-level system, with the atoms have a angular quantum number $J = 0$ for the ground state, and $J' = 1$ for the excited state. An inhomogeneous magnetic field $\mathbf{B}(x) = bx\hat{x}$ splits the energy level of the excited state into the magnetic sublevels, called the Zeeman states. By controlling the polarization of the two beams used for optical molasses, so they have opposite circular polarization, creates the Zeeman states in a useful way configuration. The energy of the $m_{J'} = -1$ and $m_{J'} = +1$ Zeeman state will be position dependent, see figure 5. The energy difference of the ground state and excited state is given by:

$$\Delta E(x) = g_{J'}\mu_B m_{J'} bx \tag{1.8}$$

where $g_{J'}$ is the Landé factor of the excited state, μ_B is the Bohr magneton and b is the
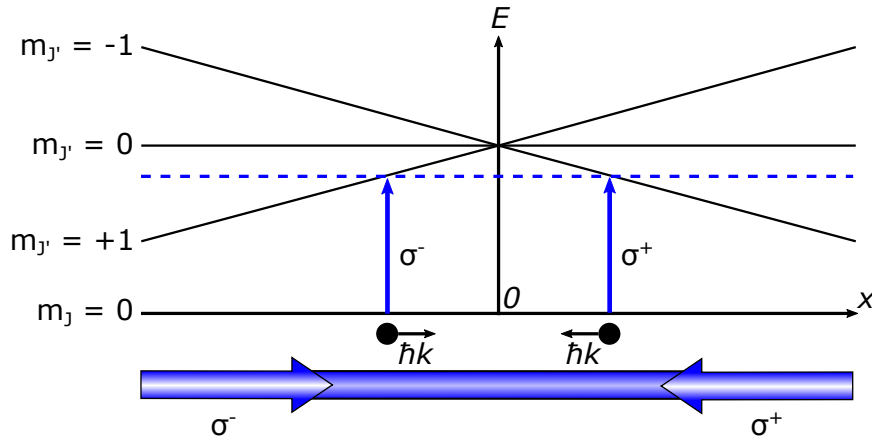
Figure 5: A two-level atomic system in the presence of ta magnetic field.

magnetic field gradient, which is chosen such that $g_{J'}b > 0$. Because of the selection rules for absorption of polarized light, an atom a positive x-position will be more likely to absorb a photon with σ^- polarization than a photon with σ^+ polarization. As a result, the atom will most likely be excited to the $m_{J'} = -1$ state, as that frequency is closer to that resonance, and experience a force pushing it towards the center. The same argument holds for an atom at a negative x-position, where it will preferentially absorb a photon with polarization σ^+, and be excited to the $m_{J'} = +1$ state, and pushed towards the center. The Doppler shifted radiation pressure force can therefore be expanded by including the Zeeman shift and optical molasses, will result in:

$$\mathbf{F} = \hbar\mathbf{k}\frac{\gamma}{2}\left[\frac{\frac{I}{I_{sat}}}{1 + \frac{4(\omega - \omega_0 - kv - g_{J'}\mu_B bx/\hbar)^2}{\gamma^2}} - \frac{\frac{I}{I_{sat}}}{1 + \frac{4(\omega - \omega_0 + kv + g_{J'}\mu_B bx/\hbar)^2}{\gamma^2}}\right] \quad (1.9)$$

This one-dimensional example can be further expanded to a three-dimensional case, with three pairs of counter-propagating beams, each pair orthogonal to each other, intersecting at the region of zero magnetic field. The temperature limit of cooling with this scheme is the Doppler temperature, given by:

$$T_D = \frac{\hbar\gamma}{4k_B}\frac{1 + (2\delta/\gamma)^2}{2|\delta|/\gamma} \quad (1.10)$$

with goes the its minimum when $|\delta| = \gamma/2$:

$$T_D^{\min} = \frac{\hbar\gamma}{4k_B} \quad (1.11)$$

Evidently, the lowest achievable temperature in a MOT is solely dependent on the linewidth of the transition used for cooling.

1.4   Optics

In this thesis much of the work have been on designing and characterizing the probe and control paths for use in the final experiment. To correctly characterize laser light by imaging, a thorough understanding of Gaussian optics is required. This section gives introduction to Gaussian beam, aberrations and choice of lenses.

1.4.1   Gaussian optics

Under ideal conditions a laser beam can be described as a electromagnetic radiation whose transverse magnetic and electric field amplitude profile is given by the Gaussian function. If this is the case the beam is called a Gaussian Beam [72]. As laser light is of fundamental importance for cold atom experiments, in this section Maxwell's equations will be used to deviate the propagation of light, to further understand the properties of Gaussian beams.

Light propagation in a medium is given by Maxwell's equations:

$$\vec{\nabla} \cdot \mathbf{D} = \rho \Leftrightarrow \vec{\nabla} \cdot \mathbf{E} = \frac{\rho}{\epsilon_r \epsilon_0} \qquad\qquad \text{Gauss's law} \qquad (1.12)$$

$$\vec{\nabla} \cdot \mathbf{B} = 0 \qquad\qquad \text{Gauss's law of magnetism} \qquad (1.13)$$

$$\vec{\nabla} \times \mathbf{E} = -\frac{\partial \mathbf{B}}{\partial t} \qquad\qquad \text{Maxwell-Faraday's law} \qquad (1.14)$$

$$\vec{\nabla} \times \mathbf{H} = \mathbf{J} + \frac{\partial \mathbf{D}}{\partial t} \Leftrightarrow \vec{\nabla} \times \mathbf{B} = \mu_r \mu_0 \mathbf{J} + \frac{n^2}{c^2}\frac{\partial \mathbf{E}}{\partial t} \qquad \text{Maxwell-Ampere's law} \qquad (1.15)$$

where $\mathbf{D}$ is the electric displacement field, $\mathbf{E}$ the electric field, $\mathbf{H}$ the magnetic field. $\mathbf{B}$ is the magnetic flux density, also refered to as the magnetic field, $\mathbf{J}$ is the free current density, ρ is the charge density, ϵ_0 the permittivity of vacuum, ϵ_r is the dielectric constant, μ_0 permeability,μ_r the relative permeability, $n = \sqrt{\epsilon_r \mu_r}$ the refractive index of the medium, and $d = \frac{1}{\sqrt{\epsilon_0 \epsilon_r}}$ the speed of light in vacuum. The speed of light in the medium is given by $v = \frac{c}{n}$. The wave equation can be derived by applying the curl operator on Maxwell-Faraday's law, under the assumption that there is no free charger $\rho = 0$ and no free currents $\mathbf{J} = 0$. By using Gauss's law, Maxwell-Ampère's law and the Jacobi identity the wave equation is obtained:

$$\vec{\nabla} \times \vec{\nabla} \times \mathbf{E} = -\vec{\nabla} \times \frac{\partial \mathbf{B}}{\partial t}$$

$$\vec{\nabla}(\vec{\nabla} \cdot \mathbf{E}) - \vec{\nabla}^2 \mathbf{E} = -\vec{\nabla} \times \frac{\partial}{\partial t}(\vec{\nabla} \times \mathbf{B})$$

$$\vec{\nabla}^2 \mathbf{E} = \frac{1}{v^2}\frac{\partial^2 \mathbf{E}}{\partial t^2} \qquad\qquad (1.16)$$

Any function that satisfies equation (1.16) is therefore a possible optical wave. By expressing the electric field in terms of a complex electric field $\widetilde{\mathbf{E}}$, where the real part of the field is the

physical quantity:

$$\mathbf{E} = \mathrm{Re}\left(\widetilde{\mathbf{E}}\right) = \frac{1}{2}\left(\widetilde{\mathbf{E}} + \widetilde{\mathbf{E}}^*\right) \tag{1.17}$$

The polarization of the electric field is taken as being linear for simplicity. The complex electric field can be expressed as the complex amplitude $\widetilde{E}(\mathbf{r})$ [72]:

$$\widetilde{E}(\mathbf{r},t) = \widetilde{E}(\mathbf{r})e^{i\omega t} \tag{1.18}$$

where $\mathbf{r}$ is the spatial coordinate, t is the time and ω the angular frequency. Putting the complex amplitude into the wave equation to obtain the Helmholtz wave equation, it is seen that:

$$\vec{\nabla}^2 \widetilde{E}(\mathbf{r})e^{i\omega t} = \frac{1}{v^2}\frac{\partial^2}{\partial t^2}\widetilde{E}(\mathbf{r})e^{i\omega t}$$

$$\vec{\nabla}^2 \widetilde{E}(\mathbf{r})e^{i\omega t} = -\frac{\omega^2}{v^2}\widetilde{E}(\mathbf{r})e^{i\omega t}$$

$$(\vec{\nabla}^2 + k^2)\widetilde{E}(\mathbf{r}) = 0 \tag{1.19}$$

where $k = \omega/v = 2\pi/\lambda$ is the wavenumber, $\lambda = \lambda_0/n$ is the wavelength in the medium and λ_0 is the wavelength in vacuum. The simplest solution to the Helmholtz equation is that of a plane wave: $\widetilde{E}(\mathbf{r}) = E_0 e^{-i\mathbf{k}\cdot\mathbf{r}}$, where E_0 is called the complex envelope. Inserting this expression into the complex amplitude gives:

$$\widetilde{E}(\mathbf{r},t) = E_0 e^{i(\omega t - \mathbf{k}\cdot\mathbf{r})} \tag{1.20}$$

As discussed later in this section the intensity of an optical wave is proportional to the time-average squared electric field $I = |E_0|^2$. This make the intensity of a plane wave constant everywhere in space, and consequently the plane will carry infinite power, making the solution non-physical [72].

Another solution for the Helmholtz wave equation is the spherical wave. In this case the complex amplitude becomes $\widetilde{E}(\mathbf{r},t) = E_0 e^{i(\omega t - \mathbf{k}\cdot\mathbf{r})}$, where r is the distance from origin, and k is the wave vector modulus. The intensity goes as $I = \frac{|E_0|^2}{r^2}$, which means that when the distance r goes to zero, the intensity and electric field goes to infinity, making the spherical wave a singular solution at this point. Both the plane and spherical wave are somewhat extreme cases, and evidently none of them are very good at describing a laser beam.

A third possibility is a paraxial wave. The wave is centred around the axis of propagation and where the wave front normals makes small angles to the axis. The complex amplitude is:

$$\widetilde{E}(\mathbf{r}) = A(\mathbf{r})e^{-ikz} \tag{1.21}$$

The complex envelope $A(\mathbf{r})$ is assumed to be a slowly varying function with respect to the position z. Therefore a displace $\Delta z = \lambda$ contains a change in the envelope much smaller than the envelope itself $\Delta A(\mathbf{r}) \ll A(\mathbf{r})$. By inserting the paraxial wave into the Helmholtz equation the following is obtained:

$$
\begin{aligned}
0 &= (\vec{\nabla}^2 + k^2)A(\mathbf{r})e^{-ikz} \\
&= \left(\frac{\partial^2}{\partial x^2} + \frac{\partial^2}{\partial y^2}\right)A(\mathbf{r})e^{-ikz} + \frac{\partial^2}{\partial z^2}\left(A(\mathbf{r})e^{-ikz}\right) + k^2 A(\mathbf{r})e^{-i\mathbf{k}z} \\
&= \left(\frac{\partial^2}{\partial x^2} + \frac{\partial^2}{\partial y^2}\right)A(\mathbf{r})e^{-ikz} + \frac{\partial}{\partial z}\left(\frac{\partial A(\mathbf{r})}{\partial z}e^{-ikz} - ikA(\mathbf{r})e^{-ikz}\right) + k^2 A(\mathbf{r})e^{-i\mathbf{k}z} \\
&= \left(\frac{\partial^2}{\partial x^2} + \frac{\partial^2}{\partial y^2}\right)A(\mathbf{r})e^{-ikz} + \frac{\partial^2 A(\mathbf{r})}{\partial z^2}e^{-ikz} - 2ik\frac{\partial A(\mathbf{r})}{\partial z}e^{-ikz} - k^2 A(\mathbf{r})e^{-i\mathbf{k}z} + k^2 A(\mathbf{r})e^{-i\mathbf{k}z} \\
&= \left(\frac{\partial^2}{\partial x^2} + \frac{\partial^2}{\partial y^2}\right)A(\mathbf{r})e^{-ikz} + \frac{\partial^2 A(\mathbf{r})}{\partial z^2}e^{-ikz} - 2ik\frac{\partial A(\mathbf{r})}{\partial z}e^{-ikz} \quad (1.22)
\end{aligned}
$$

To further reduce this expression, it is assumed that $\Delta z = \lambda$ and $\Delta A(\mathbf{r}) \ll A(\mathbf{r})$, which leads to the following inequalities for the first and second derivative:

$$
\Delta A(\mathbf{r}) = \frac{\partial A(\mathbf{r})}{\partial z}\Delta z = \frac{\partial A(\mathbf{r})}{\partial z}\lambda = \frac{\partial A(\mathbf{r})}{\partial z}\frac{2\pi}{k} \ll A(\mathbf{r}) \qquad \Rightarrow \frac{\partial A(\mathbf{r})}{\partial z} \ll kA(\mathbf{r})
$$

$$
\Delta\frac{\partial^2 A(\mathbf{r})}{\partial z} = \frac{\partial^2 A(\mathbf{r})}{\partial z^2}\Delta z = \frac{2\pi}{k}\frac{\partial^2 A(\mathbf{r})}{\partial z^2} \ll \Delta(kA(\mathbf{r})) = k\Delta A(\mathbf{r}) \qquad \Rightarrow \frac{\partial^2 A(\mathbf{r})}{\partial z^2} \ll k^2 A(\mathbf{r})
$$

The second derivative can be completely neglected, as the change in the envelope itself is very small. By using the transverse Laplacian operator $\nabla_T^2 = (\frac{\partial^2}{\partial x^2} + \frac{\partial^2}{\partial y^2})$, the paraxial Helmholtz equation can be further reduced to:

$$
\nabla_T^2 A(\mathbf{r}) - 2ik\frac{\partial A(\mathbf{r})}{\partial z} = 0 \quad (1.23)
$$

A trial solution to the paraxial Helmholtz equation is:

$$
A(\mathbf{r}) = E_0 e^{-i\left(p(z)+k\frac{\rho^2}{2q(z)}\right)} \quad (1.24)
$$

where $\rho^2 = x^2 + y^2$ is the radial distance squared. Combining the trial solution and the paraxial Helmholtz equation gives:

$$
\begin{aligned}
\nabla_T^2 E_0 e^{-i\left(p(z)+k\rho^2/(2q(z))\right)} - 2ik\frac{\partial}{\partial z}\left(A(\mathbf{r}) = E_0 e^{-i\left(p(z)+k\rho^2/(2q(z))\right)}\right) &= 0 \\
A(\mathbf{r})\left(\frac{-2ik}{q(z)} - \frac{k^2\rho^2}{q^2(z)} - 2k\frac{\partial p(z)}{\partial z} + \frac{k^2\rho^2}{q^2(z)}\frac{\partial p(z)}{\partial z}\right) &= 0 \\
A(\mathbf{r})\left[\frac{k^2\rho^2}{q^2(z)}\left(\frac{\partial q(z)}{\partial z} - 1\right) - 2k\left(\frac{i}{q(z)} + \frac{\partial p(z)}{\partial z}\right)\right] &= 0 \quad (1.25)
\end{aligned}
$$

Both terms in equation (1.25) is dependent on the position z, and the second term depend on radial distance as well. Solving the two differential equations will provide information about the two functions $p(z)$ and $q(z)$.

Starting with $q(z)$, the solution to the differential equation is $q(z) = z + c$, where c is a constant. If c is real the trial solution is a parabolic wave, and if c is a complex number, $c = iz_R$, the trial solution is a Gaussian beam. This can be shown by setting $z = 0$ and replacing $q(c)$ with iz_R in equation (1.24). The constant z_R is known a the Rayleigh length. The term $e^{-ik\frac{\rho^2}{2q(z)}}$ becomes $e^{-\frac{\rho^2 k}{2z_R}}$ which is a Gaussian.

To find the amplitude and phase of the trial solution of the paraxial Helmholtz equation, it is useful to define the complex curvature of the radius, given by $q(z) = z + iz_R$. It's inverse can be used to find the imaginary and real part [72]:

$$\frac{1}{q(z)} = \frac{1}{z + iz_R} = \frac{1}{r(z)} - i\frac{\lambda}{\pi w(z)^2} \tag{1.26}$$

The meaning of the two introduced variables $w(z)$ and $r(z)$ can be found by inspecting the imaginary and real parts of of the trial solution of the paraxial Helmholtz equation:

$$w(z)^2 = -\frac{\lambda}{\pi \operatorname{Im}[1/q(z)]} = -\frac{\lambda}{\pi \operatorname{Im}[\frac{z - iz_R}{z^2 + z_R^2}]} = \frac{\lambda(z^2 + z_R^2)}{\pi z_R} = \frac{\lambda z_R}{\pi}\left[1 + \left(\frac{z}{z_R}^2\right)\right] \tag{1.27}$$

$$w(z) = w_0\sqrt{1 + \left(\frac{z}{z_R}^2\right)} \qquad \text{with} \quad w_0 = \sqrt{\frac{\lambda z_R}{\pi}} \tag{1.28}$$

$$r(z) = \frac{1}{\operatorname{Re}[1/q(z)]} = \frac{z^2 + z_R^2}{z} = z\left[1 + \left(\frac{z}{z_R}^2\right)\right] \tag{1.29}$$

with $w_0 = \sqrt{\frac{\lambda z_R}{\pi}}$ being the minimum value of the beam radius, also called the beam waist. $w(z)$ is the beam radius and $r(z)$ is the radius of curvature of the wave front. An illustration of the Gaussian beam and the parameters can be seen on figure 6.

As illustrated on figure 6 the increasing in $w(z)$ is approximate linear when $z \gg z_R$. The angle between the linear regression an the z-axis is defined as the angular divergence, which for a angle beam is $\theta = \frac{w_0}{z_R} = \frac{\lambda}{\pi w_0}$. As the beam divergence is inversely proportional with the beam waist.

Another important parameter is the depth of focus, which is 2 times the Rayleigh length, $2z_R = \frac{2\pi w_0}{\lambda}$. The depth of focus is proportional with the waist, and inversely proportional with the wavelength. This works in favour of the near ultra-violet wavelength used for both probe and control light of Yb. Looking at the radius of the curvature in extreme cases, as $r(z \to z_0)$ and $r(z \to \infty)$, it is seen that in both cases $r(z) \to \infty$. This means that the curvature of the wave fronts are planar and the Gaussian beam behaves as a planar wave at these extremes. For light between between this two extremes, the Gaussian have a finite
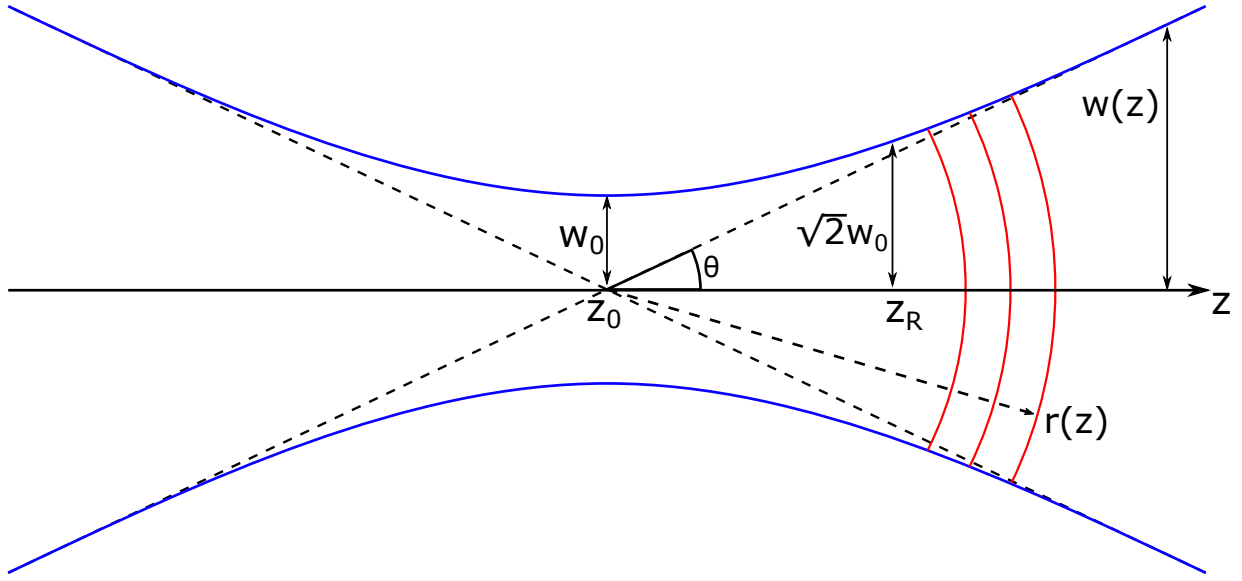
Figure 6: Illustration of some of the important parameters of a Gaussian beam.

curvature, with maximum curvature at $z = z_R$, so for points $z \gg z_R$ the beam takes the form of a spherical wave.

The second differential equation in equation (1.22) shows the meaning of $p(z)$:

$$\frac{dp(z)}{dz} = -\frac{i}{q(z)}$$

$$ip(z) = \int_0^z \frac{1}{z' + iz_R} = \ln(z' + iz_R)|_0^z = \ln(z + iz_R) - \ln(iz_R)$$

$$ip(z) = \ln\left[1 - i\left(\frac{z}{z_R}\right)\right] = \ln\left[\sqrt{1 + i\left(\frac{z}{z_R}\right)^2} e^{-i\tan^{-1}(z/z_R)}\right]$$

$$ip(z) = \ln\left[\sqrt{1 + i\left(\frac{z}{z_R}\right)^2}\right] - i\tan^{-1}\left(\frac{z}{z_R}\right)$$

$$e^{-ip(z)} = \frac{1}{\sqrt{1 + \left(\frac{z}{z_R}\right)^2}} e^{i\tan^{-1}\left(\frac{z}{z_R}\right)} = \frac{w_0}{w(z)} e^{i\tan^{-1}\left(\frac{z}{z_R}\right)} = \frac{w_0}{w(z)} ei\zeta(z) \tag{1.30}$$

It is seen that $p(z)$ is gives an additional phase term $\zeta(z)$, which is know as the Gouy phase. This term corresponds to the phase retardation, which is in the range $\frac{-\pi}{2}$ to $\frac{+\pi}{2}$ when going from $z = -\infty$ to $z = +\infty$. Inserting the complex envelope $A(\mathbf{r})$ into the complex amplitude, as seen in equation (1.21), together with relations for $q(z)$ and $p(z)$, the full expression for the Gaussian beam is found:

$$\widetilde{E}(\rho, z) = \frac{E_0 w_0}{w(z)} e^{-\frac{\rho^2}{w(z)^2}} e^{-i\left(kz + \frac{k\rho^2}{2r(z)} - \zeta(z)\right)} \tag{1.31}$$

The first exponential term is the spatial Gaussian shape of the beam and the second exponetial term is for the phase.

The intensity of the beam is a physical measurable quantity, which can be estimated by:

$$I(\rho,z,t) = \epsilon_0 c \left\langle \text{Re}[\widetilde{E}(\rho,z,t)]^2 \right\rangle_T \tag{1.32}$$

with ϵ_0 being the permittivity in free space, c the speed of light in vacuum. $\langle \ldots \rangle_T$ denotes time averaging, at a scale larger than the optical cycle. By inserting equation (1.17) into equation (1.32), the intensity can be written as:

$$
\begin{aligned}
I(\rho,z,t) &= \epsilon_0 c \left\langle \left[\frac{1}{2} \left(\widetilde{E}(\rho,z,t) + \widetilde{E}^*(\rho,z,t) \right) \right]^2 \right\rangle_T \\
&= \frac{\epsilon_0 c}{4} \left[\left\langle \widetilde{E}(\rho,z,t)^2 \right\rangle_T + \left\langle \widetilde{E}^*(\rho,z,t)^2 \right\rangle_T + 2 \left\langle |\widetilde{E}(\rho,z,t)|^2 \right\rangle_T \right] \\
&= \frac{\epsilon_0 c}{2} \left\langle \widetilde{E}(\rho,z,t)^2 \right\rangle_T \\
&= \frac{E_0 \epsilon_0 c}{2} \frac{w_0^2}{w(z)^2} e^{-\frac{2\rho^2}{w(z)^2}}
\end{aligned}
\tag{1.33}
$$

as $\left\langle \widetilde{E}(\rho,z,t)^2 \right\rangle_T = 0$ and $\left\langle \widetilde{E}^*(\rho,z,t)^2 \right\rangle_T = 0$. Defining the maximum intensity as $I_0 = \frac{E_0 \epsilon_0 c}{2}$ the Gaussian beam intensity becomes:

$$I(\rho,z) = I_0 \frac{w_0^2}{w(z)^2} e^{-\frac{2\rho^2}{w(z)^2}} \tag{1.34}$$

The intensity is highest at $\rho = 0$, and falls by a factor $1/e^2$ when $\rho = w(z)$. The optical power of the Gaussian beam goes over an area with radius ρ is:

$$
\begin{aligned}
P(\rho,z) &= 2\pi \int_0^\rho \rho' I(\rho',z) d\rho' = 2\pi I_0 \frac{w_0^2}{w(z)^2} \int_0^\rho \rho' e^{-\frac{2\rho'^2}{w(z)^2}} d\rho' \\
P(\rho,z) &= 2\pi I_0 \frac{w_0^2}{w(z)^2} \int_0^{s(\rho)} \frac{w(z)^2 \rho'}{4\rho'} e^{-s} ds = \frac{\pi I_0 w_0^2}{2} \left(1 - e^{-\frac{2\rho^2}{w(z)^2}} \right) \\
P(\rho,z) &= P_0 \left(1 - e^{-\frac{2\rho^2}{w(z)^2}} \right)
\end{aligned}
\tag{1.35}
$$

where the maximum power is $P_0 = \frac{\pi I_0 w_0^2}{2}$. For a circle the with radius $\rho = w(z)$ the power is $1 - \frac{1}{e^2} \approx 0.865$ of the maximum intensity.

It is important to point out that the Gaussian beam solution shown in this section, is only one of many possible solutions to the paraxial Helmholtz equation. The Gaussian beam belongs to a group of solutions called Hermite-Gaussian beams, where the Gaussian beam is the the so-called fundamental mode. Other higher-order modes beside Hermite-Gaussian also exist.

The output of a laser does not necessarily consist of only the fundamental mode, where a factor M^2 are used to specify the quality of the laser beam. A pure Gaussian beam will have an M^2 of one, and the factor will increase with the presence of other modes.

1.4.2   Aberrations and choice of lenses

Aberration in a optical system causes light to be spread out spatially, rather than being focused to a point. Aberrations are classified into chromatic and achromatic aberration. Chromatic aberration is caused by the fact that the refractive index of some materials are dependent of the wavelength of light, so unless a optical system specifically have been designed to compensate for this, light at different wavelength will not focus to the same point. This kind of aberration is usually not a great concern when working with laser, due the monochromaticity of laser light.

The major types of monochromatic aberration are: Spherical aberrations, coma, astigmatism, curvature of field and distortion. Spherical aberrations are usually caused by spherical lenses, as the curvature and therefore the incident angle of the light on the lens, changes from being orthogonal at the center and becomes more angled when moving radially outwards. This effect becomes more pronounced the larger the beam is on the lens. Some lenses are specifically designed to minimize this effect by having the curvature of the lens being aspherical. Comatic aberration is caused by light being refracted differently at various zones of the lens, so when a light beam hits the lens at an angle, a perfectly collimated beam will appear oblique after the lens. Astigmatism results from the failure of a single zone of the lens to focus the image of an off-axis point to a single point. Curvature of field stems from the fact the imaging an object perpendicular to the optical axis, will result in an paraboloidal image surface. A flat image surface is usually needed to better match the image plane of the camera sensor. Distortion describes how magnitude in an image changes across the field of view. In the case where the magnification decreases when moving from the center and outwards is called barrel distortion. In the opposite case where the magnification increases when moving from the center and outwards is called pincushion distortion. On figure 7 the describe aberrations are illustrated.
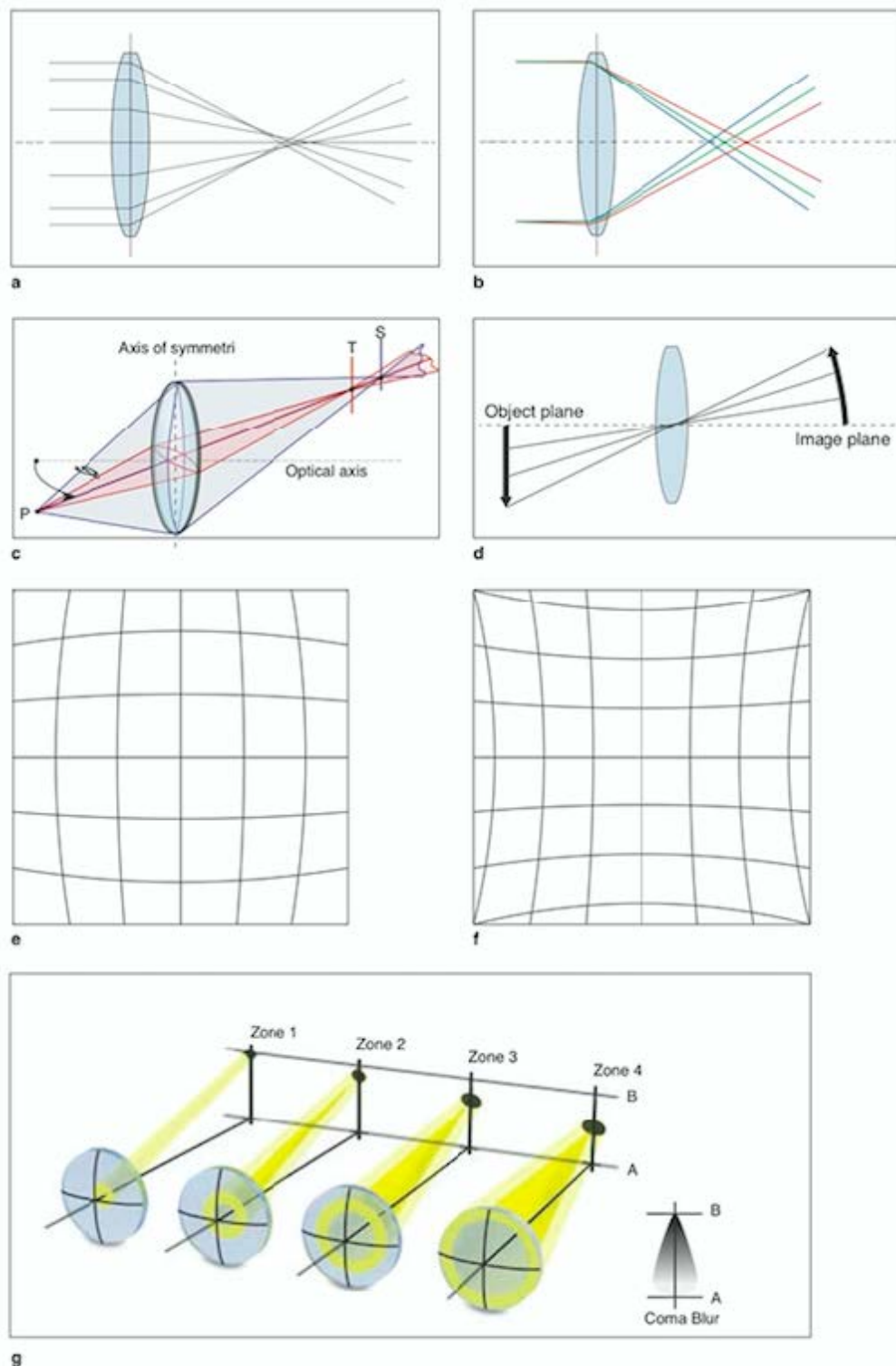
Figure 7: Illustrations of aberration. **a)** spherical aberration. **b)** chromatic aberration. **c)** astigmatic aberration. **d)** curvature of field. **e)** barrel distortion. **f)** pincushion distortion. **g)** comatic aberration. Figure from [73].

Choosing the right lens is dependent on what purpose the lens have to serve. Different factors such as price, focal length, beam size, chromaticity and more, are all factors to take into account when choosing lens.

The most simple in design, and therefore usually the cheapest, is spherical lenses. These lenses have one or both surfaces curved either inwards (called concave) or outwards (convex). They are usually used in situations where the optical performance does not have to been good, as they preform poorly by them self. They are also commonly used in more complex multi-lens systems, as their innate poor performance can be compensated by clever design.

Combining two simple spherical lens of different material gives a doublet lens. Doublet lenses are usually cemented, and because of ability to correct for chromatic aberration, are also called cemented achromats. They also preform better in regards to other aberrations compared to spherical lenses.

More complex are aspherical lenses. Contrary to the spherical lenses, the surface of aspherical lenses are not portions of a sphere or cylinder. By carefully designing the lens, it is possible to minimize the aberrations typically seen on the more simple lens types. The complexity of the manufacturing process however increases the price of aspheres.

By combining multiple lenses different kinds of manipulations can be done that a beam. One of the most simple combinations is placing two lens apart, with the distance between them being equal to the sum of their focal lengths. If the focal length of the two lenses are different, a collimated beam will either be enlarged or reduced depending on the ratio of the focal length of the lenses. This is the concept behind microscopes, where a set of two or more lenses magnify to an image.

For this experiment aspheric lenses was bought for coupling beams into optical fibers, and for collimating the light coming out of the fibers. Ab achromatic lens were chosen for the probe lens because differing wavelength is used for the probe and control beam. As shown in chapter 3.2.1, the performance of the bought aspheres are shown to be of subpar quality, leading to using an achromat for outcoupler the probe lens as well.

2 Our New Ytterbium Experiment

This chapter presents the design of our new ytterbium experiment. The experimental setup consist of two major part; A 2D MOT chamber for transversally loading ytterbium atoms, and a ultra-high vacuum science chamber with a 3D MOT for atom trapping. All major design decisions has been made by post-Doc Simon Ball, and master student Philipp Lunt. For a more detailed discussing of the design decisions made, see master thesis by Philipp Lunt [74].
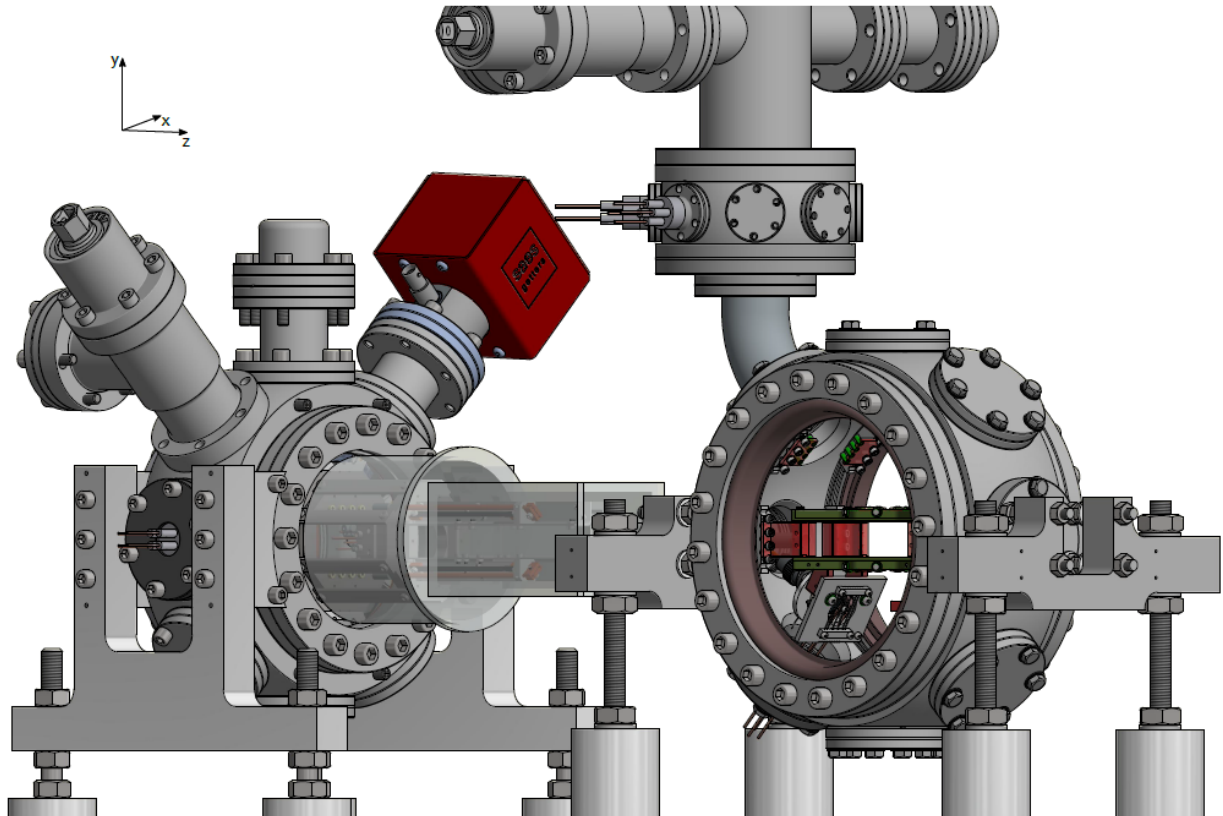

Figure 8: CAD model for the experiment, image from [74].

2.1 Vacuum chambers

To achieve ultra-high vacuum necessary to study non-linear quantum optics, a common solution is a two chamber system [75] where atoms are loaded in a lower vacuum, and then transferred to a high vacuum chamber. Transportation can of the atoms from one chamber to the other can be facilitated by different methods, including spatially moving the magnetic trap potential [76], by using a Zeeman slower [77], or a 2D MOT [78].

Since it is difficult to load ytterbium atoms from a background gas, because of its low vapour

pressure, a 2D MOT with four ytterbium dispenser[1] was designed (see figure **??**). A 2D MOT setup is both more simple and compact than a Zeeman slower, and with similar loading rates [79]. The compactness of 2D mot with dispensers, allows it to be positioned inside a custom made double-ended Borosilicat glass cell from *Japan Cell*.

For creating the magnetic field need for the 2D MOT, permanent magnets are used. This approach is much more simple than electro magnets as it requires no cooling, no electronic controls and takes up less space. By stacking magnets[2], it is possible to reach a magnetic field gradient of 50 G/cm. In the center of the 2D MOT the magnetic field gradient is 0.076 G/cm.

The 2D MOT chamber are positioned such that the transversal axis are horizontal. This makes the optics alignment around the chamber, and connecting it to the science chamber easier. To connect the 2D MOT with the science chamber a differential pumping stage are used. The differential pumping stage have a diameter of 7mm and a length of 150mm making the pressure ratio between the two chambers around 300. Each chamber are connected with a vacuum pump[3].

The main part of the science chamber is the electric field control. The electric field control is used for fine control of any stray electric fields that would affect the Rydberg atoms in the chamber. Also it can induce Stark shifts, and are useful for detecting ionized Rydberg atoms. It is mounted in the center of the chamber, with good optical access given by large viewports.

The 3D MOT of the science chamber consist of two overlapped beams, in a so-called shell-MOT configuration, with the shell of the beam being at 399 nm, and the core being at 556 nm. The advantage of this configuration is the shell of the beam addresses higher velocity classes atoms, up to 40 m/s, coming from 2D MOT than would be impossible with only a 556 nm beam. The core of the beam can however cool the Yb to a much lower Doppler temperature, as the transition is narrower than the 399 nm transition, being $T_D^{\min} = \frac{\hbar\gamma}{4k_B} = 4.4\mu$K.

---

[1]Alfavacuo 3mm S-type AS-3-Yb-0500

[2]Eclipse magnets N750-RB

[3]Science chamber: Saes group NEXTorr D500; 2D MOT chamber: Saes group NEXTorr Z200

2.2   Layout of laser table

The laser system consists of 6 Toptica lasers which can be seen in table 2 with name, type, wavelength and purpose. The master laser is used as a frequency reference for DL 1, DL 2 and the MOT cooler by offset-locking [80]. The frequency of the master laser is itself locked to a high-finesse reference cavity. The 3D MOT laser is used for cooling the atoms in the science chamber and are locked to the cavity as well. The MOT laser is used for cooling in the 2D MOT and cooling in the 3D MOT in a core-shell-MOT configuration to increase the capture velocity. The MOT laser can additionally be used as a push beam to increase the flux of atoms from the 2D MOT to the science chamber. The DL 1 is used for probing the atoms in the science chamber from their ground state to the intermediate state. The high intensity Rydberg laser will excite the probed atoms from the intermediate state to a Rydberg state. The Rydberg laser is frequency locked to the high-finesse cavity. The DL 2 will be used for imaging the atomic cloud about the atomic cloud density and temperature.

Name	Laser	Wavelength [nm]	Purpose
Master Laser	Toptica DL-SHG pro	399, 798	Frequency reference
Rydberg Laser	Toptica TA-SHG pro	395, 790	Rydberg excitation
3D MOT Laser	Toptica TA-SHG pro	556, 1112	Cooling
MOT Laser	Toptica TA-SHG pro	399, 798	Cooling, (push beam)
DL 1	Toptica DL pro	399	Probing, imaging
DL 2	Toptica DL pro	399	Probing, imaging

Table 2: All laser are commercial tunable diode lasers (DL). The Master, Rydberg, 3D MOT and MOT laser have a single harmonic generation (SHG) stage, and the three latter laser are also equipped with a high power taperred amplifier (TA).

On figure 9 the layout of the laser table is shown. All beamspaths are in a height of 5 cm above the table, expect for the beam paths around the cavity, and the 3D MOT laser. Around the cavity the height is set by the cavity mirrors, which is 12.7 cm. The 3D MOT laser is mounted on top of a closed-loop cooler for thermal stability, which raises the laser module, and thereby the beam height, to a total beam height of 7.5 cm. The lasers are all connected to a wavemeter[4]. For the SHG lasers, the measured wavelength is of their infrared seed lasers.
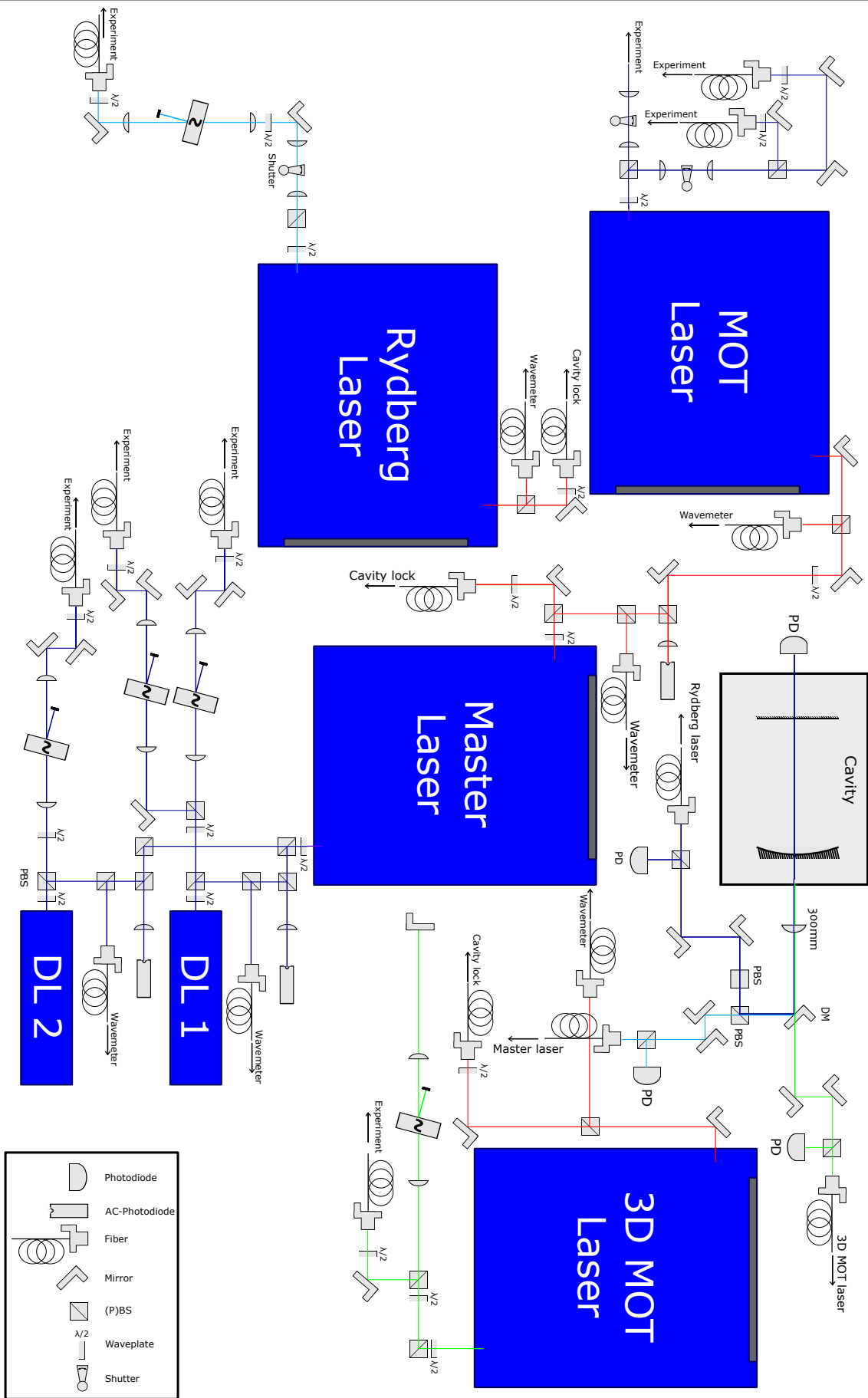
---

[4]High Finesse WS-5

Figure 9: Setup of laser table. Figure from [74].

In front of DL 1 and 2 AOMs[5] are placed for fast intensity shaping and switching. The beams are then coupled into fibers taking it to the experiment table. As the experiment table and the laser table are two separate tables, any spatial drift between them will lead to misalignment of optics. In theory the fibers should also act as mode filters, only allowing the fundamental transversal Guassian mode to be taken to the experiment. Work done in the laboratory however shows signs of trouble, see chapter 3.2.

The near ultra-violet light from the MOT laser is divided into three branches. One branch for the 2D MOT. A second branch for the two-color shell MOT in the science chamber. The last branch eventually be used for a push beam, if needs arises.

For locking the MOT laser and DL 1 and 2, they are each overlapped with the master laser for offset locking. The MOT laser are locked its infrared seed laser to the infrared seed laser of the Master laser. DL 1 and 2 are locked to the near ultra-violet laser of the Master laser. The overlapped beams are focused on fast AC-photodiodes[6]. The signal from the photodiode is in turn processed by an electronics board[7] which realizes a digital-phase-locked loop.

Stellar work was done in characterizing the cavity locks by previous master student Philipp Lunt, which can be seen in his master thesis [74].

---

[5]Gooch & Housego AOM 3200-129
[6]Hamamatsu Photonics G4176-03
[7]Analog Devices AD4007

3 Probe/Control Setup

As describe in section **??**, an crucial part of our new ytterbium experiment is the design, implementation and characterization of the probe and control beams. The probe and control beams will excite the ytterbium to a Rydberg state. The requirement for our probe and control can be seen in table 3.

	Probe	Control
Power	Single photon level	As high power as possible
Size of beam	5-10 um	Twice as big as probe, 10-20 um
Stability	Polarization stable	Polarization stable
Separability	Must be able to effectively separate the probe and control beam	

Table 3

This narrow waist of the probe is chosen because the regime where the probe beam radius is smaller than the blockade radius is interesting for investigating many phenomena where the medium can be considered one-dimensional.

The probe light is supplied by a Toptica DL Pro laser (DLPro1) supplying light at 399 nm. DL 1 is beatnote locked to the Master Laser. Before coupling the laser into a fiber, the beam is going through a acousto-optic modulator[8] (AOM) for intensity control and shaping (see chapter 3.1 for details). A mechanical shutter is also placed in the beam path to obtain higher extinction ratio on the beam when needed.

After the AOM the beam is coupled into a polarization maintaining fiber[9]. For coupling the laser into the fiber a **??** mm aspherical lens is used, to match the mode field diameter (MFD) of the fiber, being 3.2 μm. For outcoupling a 19 mm achromatic cemented doublet is used to achieve a beam waist of 1.27 mm. See chapter 3.2 for further details. The setup of the probe and control around the experiment is illustrated on figure 10.

As the polarization of the probe and control have to be opposite, a way to separate the two beams after overlapping them is necessary. A common method is to separate the probe and control by wavelength. For ytterbium however the wavelength is 399 nm for the probe, and 395 for the control. Initial worries about it not being able to separate them by wavelength was however not necessary, as the company Lens Optics were able the make a filter with the needed specifications. The wavelength dependence of said filter can be seen on figure 11.

On figure 12 the polarization of one set of the probe and control are seen. The s- and p-polarization are relative to the experiment table. Relative to the beams them self, the circular

---

[8]Gooch & Housego AOM 3200-129
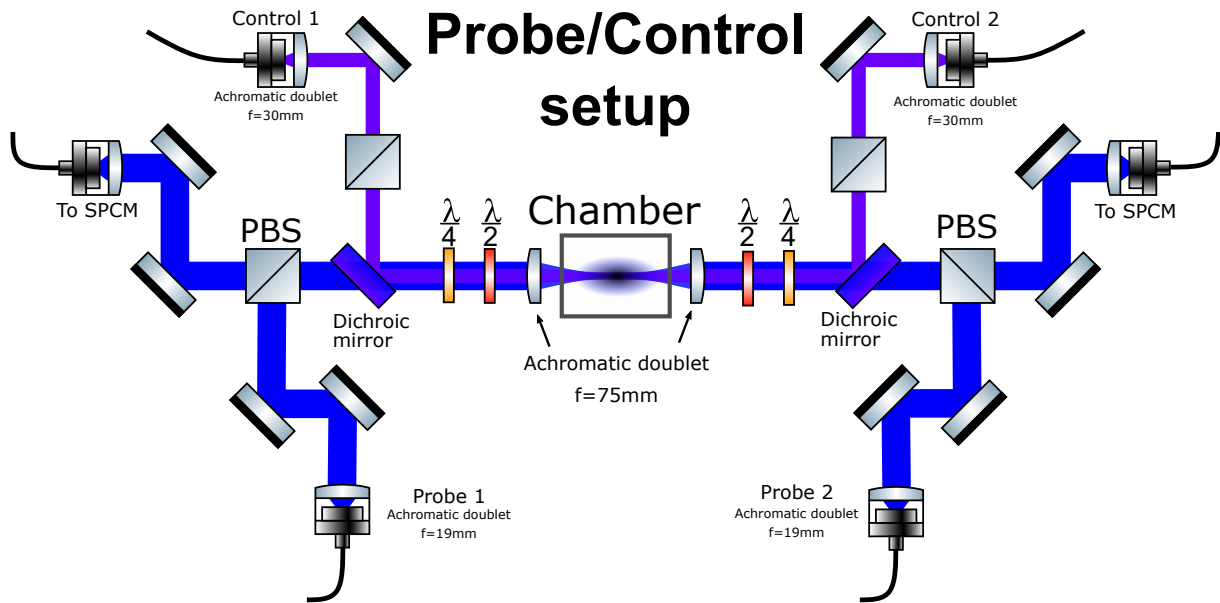[9]OZ OPTICS: QPMJ-3A3A-400-3/125-3-5-1

Figure 10: The probe and control setup for the new ytterbium experiment.

polarization of the two beams are set to be the same inside the chamber. The atoms will however experience opposite polarization of the two beams, due to their propagation being opposite. This setup ensures that the minimum amount of photons after the chamber is lost, and the maximum amount of light from the control are reaching the atom cloud.

After the chamber, the beam will be split up by the dichroic filter, and the probe light will be let to a setup of single photon counting modules (SPCM) in an extension of a Hanbury Brown and Twiss setup. This last step is not covered in this thesis [81].
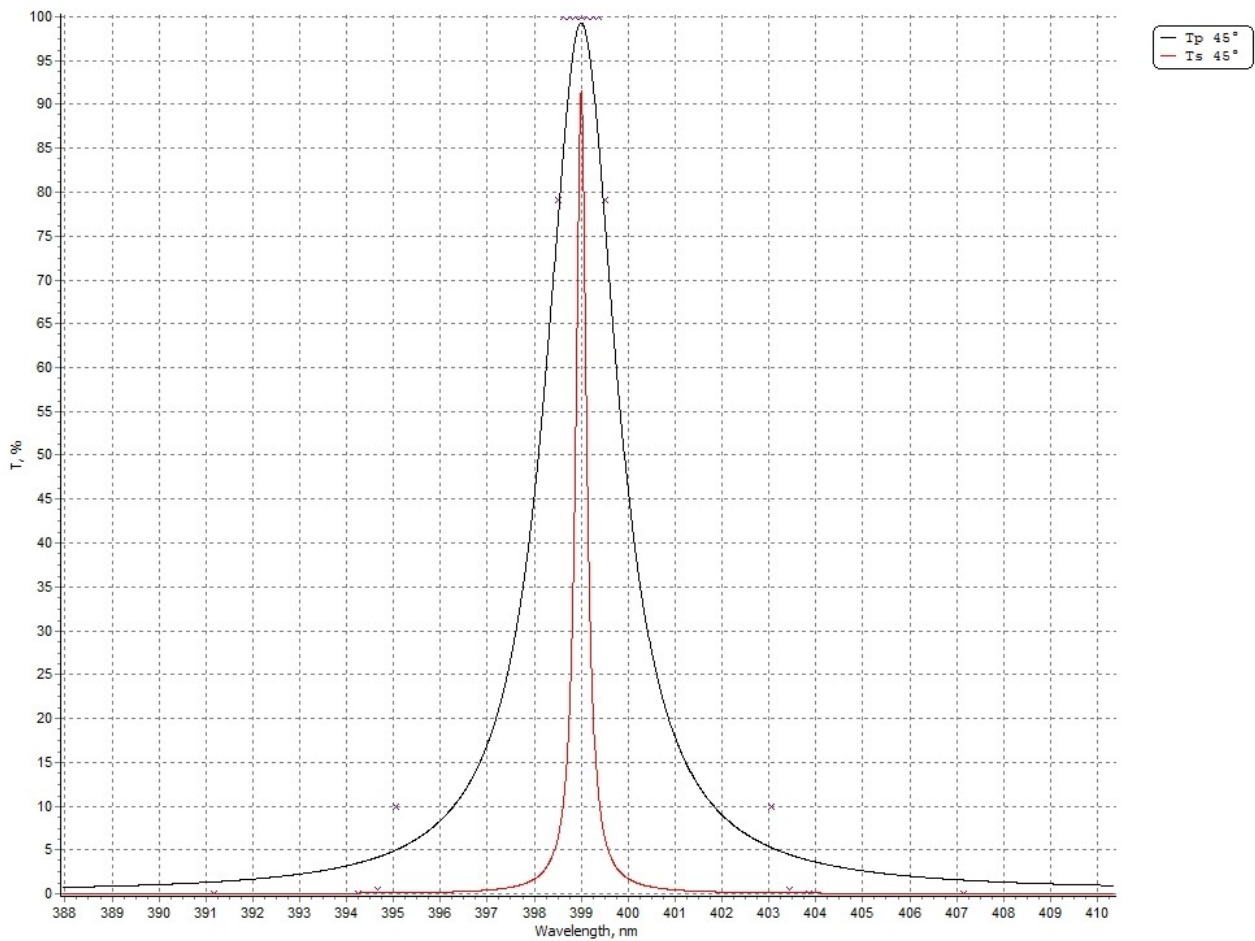
Figure 11: Dichroic filter from Lens Optics for separating probe and control beam.
Figure from specification sheet.
For 399nm $T_p = 99\%$ and $T_s = 92\%$. For 395nm $T_p = 5\%$ and $T_s = 0.2\%$.

3.1   Acousto-Optic Modulator Characterization

An Acousto-Optic Modulator (AOM), also called a Bragg cell, is device which can be used to diffract and shift the frequency of light passing through it. A piezoelectric transducer is used to create sound waves in a glass-like material. The sound waves changes the refractive index of the material, and the incoming light scatters as a result. Is the modulation can be done extremely fast, they are well suited for shaping the intensity profile of a laser beam, and can be used to switch on and off the transmission to a high degree. The interesting characteristic are:

- *Extinction ratio:* What the minimum and maximum transmission in the first order are. If this ratio is too low, it necessitate implementing a shutting in the beam path, which have a theoretical extinction ratio of infinite.
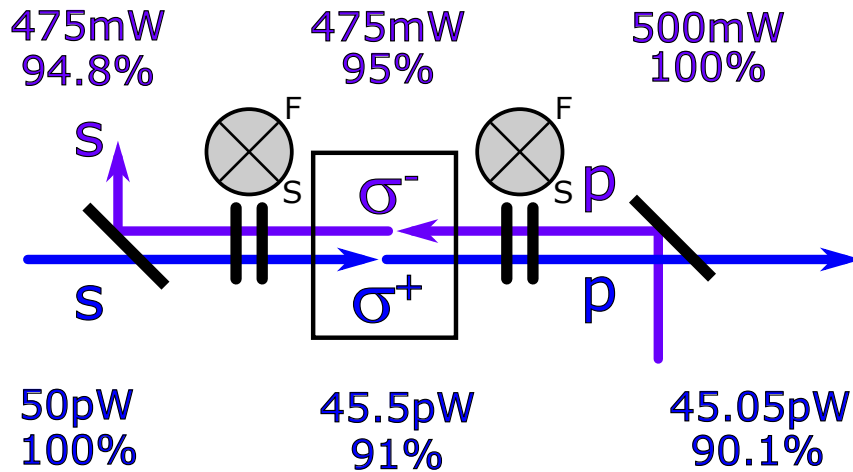
Figure 12: Polarization setup for probe 1 and control 2. The grey circles indicate the rotation of the quarter-wave plates reletive to the table, as seen from probe 1. The power is an estimate of the power of the two beams, and the percentage the power loss from the dichroic filters. The reflection is assumed to be: $R = 1 - T$.

- *Delay:* The time from sending a signal beam shape, before the AOM starts responding. The delay will need to be incorporated in the timing of the experimental cycle, when the experiment is running.

- *Rise/Fall-time:* The time it takes the AOM for going from minimum intensity in the first order at zero voltage, to the maximum intensity in the first order, and vice versa. This will put a limit on the how narrow we can make the intensity profile of the probe beam.

- *Intensity Shaping:* How well a intensity profile of the first order coming out of the AOM, correspond to the intensity profile sent to the AOM from control computer.

All these points depends upon the voltage response of the AOM, which is not linear. The best timing data taken for the AOM can be seen in table 4.

Input	Rise time[ns]	Fall time [ns]	Delay [ns]
Analog, 10V pulse	23	30	540
Digital, 3.3V pulse	12	13	500

Table 4: Rigol waveform generator. Measured on the Rigol oscilloscope. 50Ω impedance. ND=1.0 in front of incoupling lens. Averaging over 8 triggers.

Besides knowing the timing of the AOM, it is important to be able to shape the intensity of the light going through it. As seen from the voltage response, the voltage applied to the

AOM, and the intensity of the beam is not linear. It is therefore necessary to somehow map these two variables to each other. This is done with a look-up table, made from show on figure 13. It would be possible to make a polynomial fit, or otherwise interpolate the values between the measured points. This has however not been implemented, as it is deemed judged unnecessary to the degree of control we want.
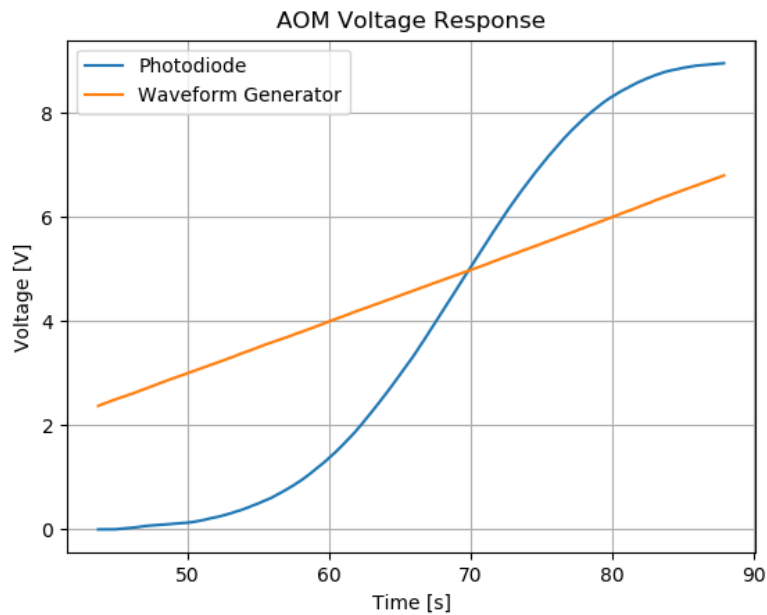

Figure 13: This is a fig of the look-up table. A Savitzky–Golay filter have been used on the data.
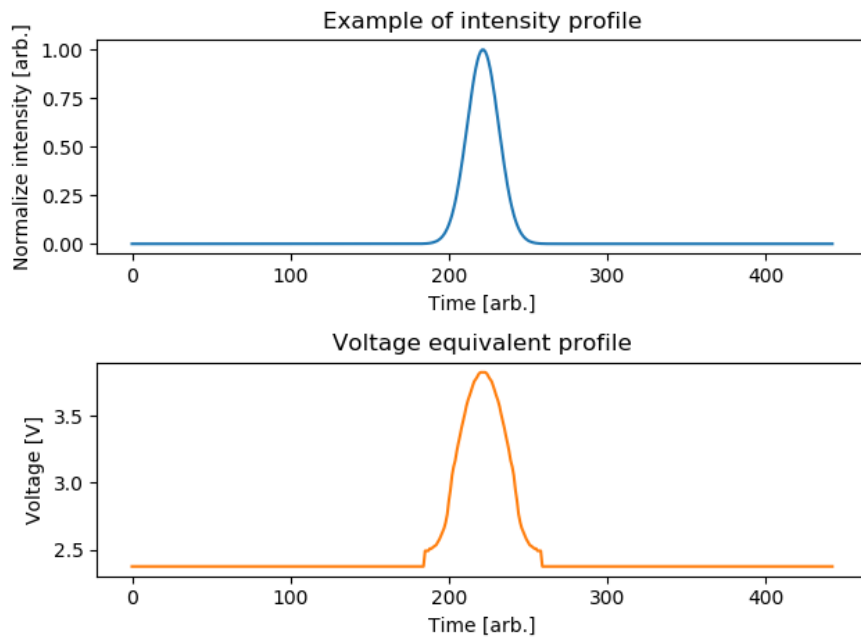
Figure 14: This is a temporary fig for the beam shaping.

3.2   Optical Fiber Characterization

A staple component of nearly all optics experiments is the optical fiber. An optical fiber is a thin transparent thread usually made of silica, used for the transportation of photons. The fiber core has a low refractive index, and are typically clad with a high refractive index material. By means of total internal reflection the light is kept in the core of the fiber. Different types of optical fibers exist.

Multi-mode(MM) fibers have a core diameter of above 10 um. This big core allows multiple light modes to propagate in the fiber. The beams are guided by total internal reflection in the core. The mode of the transmitted light will be changed compared to before the fiber. Multi-mode fibers are usually used when the mode and transmission efficiency is not crucial.

If the core of the fiber is 10 times or less than the wavelength of the transmitted light the fiber is single mode. A single-mode(SM) fiber, will only transmit one mode of the transverse modes of the light propagation in the fiber. Single-mode fibers are the most common fibers in the laboratory, as the fiber can function as a mode filter.

For polarization sensitive applications polarization-maintaining(PM) fibers are used. By taking a normal SM fiber and intentionally introducing a systematic linear birefringence in the fiber, it is possible to make the fiber polarization maintaining.

A special type of fiber is the photonic-crystal fiber (PCF). By utilizing the concept of photonic crystals, it is possible to design periodic optical nanostructures, that influence photons,

much in the same way a ionic lattices affect electrons in solids. This type of fiber can be tailored as to have specific properties, i.e. polarization maintenance, high transmission efficiency and durability.

As with all element implemented in a experiment, a thorough investigation of any optical fiber for use the in the setup is necessary. The most important characteristics to determine is:

- **Coupling efficiency** - What transmission efficiency is possible to obtain.

- **Mode** - How Gaussian the mode after the fiber looks.

- **Polarization stability** - How the polarization changes in the fiber. The polarization extinction ratio is given by $\text{PER} = 10 \log_{10} (\text{trans}_{\max}/\text{trans}_{\min})$, which is in dB.

- **Mode field diameter** - How big the core of the fiber is.

3.2.1 Beam coupling and collimation

In the scope of this thesis many different fiber couplers have been constructed and examined. Both in-couplers for coupling a collimated beam into a fiber, and out-couplers for collimating the light coming out of the fiber. This task can in some cases be considered trivial with only simple practical issues. However, as will be described in this chapter, some difficulties arose during the span of this thesis, especially concerned with the outcoupling and collimation of the probe light.

For deciding the optimal focal length f for the lens used for coupling a beam into an optical fiber, the following equation is used:

$$f = \frac{\pi D \cdot \text{MFD}}{4\lambda} \tag{3.1}$$

where D is the $1/e^2$ diameter of the beam, MFD is the mode field diameter of the fiber, and λ the wavelength of the laser. The MFD is specified by the manufacturer of the optical fiber, but usually with a fairly high tolerance. To accurately determine the MFD more precisely two methods can be used. By isolating the MFD in equation (3.1), and looking at the size of a beam collimated with a known focal length lens, the MFD can be determined.

$$\text{MFD} = \frac{4\lambda}{\pi D f} \tag{3.2}$$

The second method involves looking a the far field divergence of the naked output of the fiber. As describe in chapter 1.4.1 the divergence of the beam solely depends of the wavelength

of the light and the size of the waist. Since knowing the precise distance from the measured to the fibertip is difficult in practice, taking multiple measurements at known intervals of the diverging beam, and fitting the divergence of a Gaussian beam to said measurements, the MFD can be found.
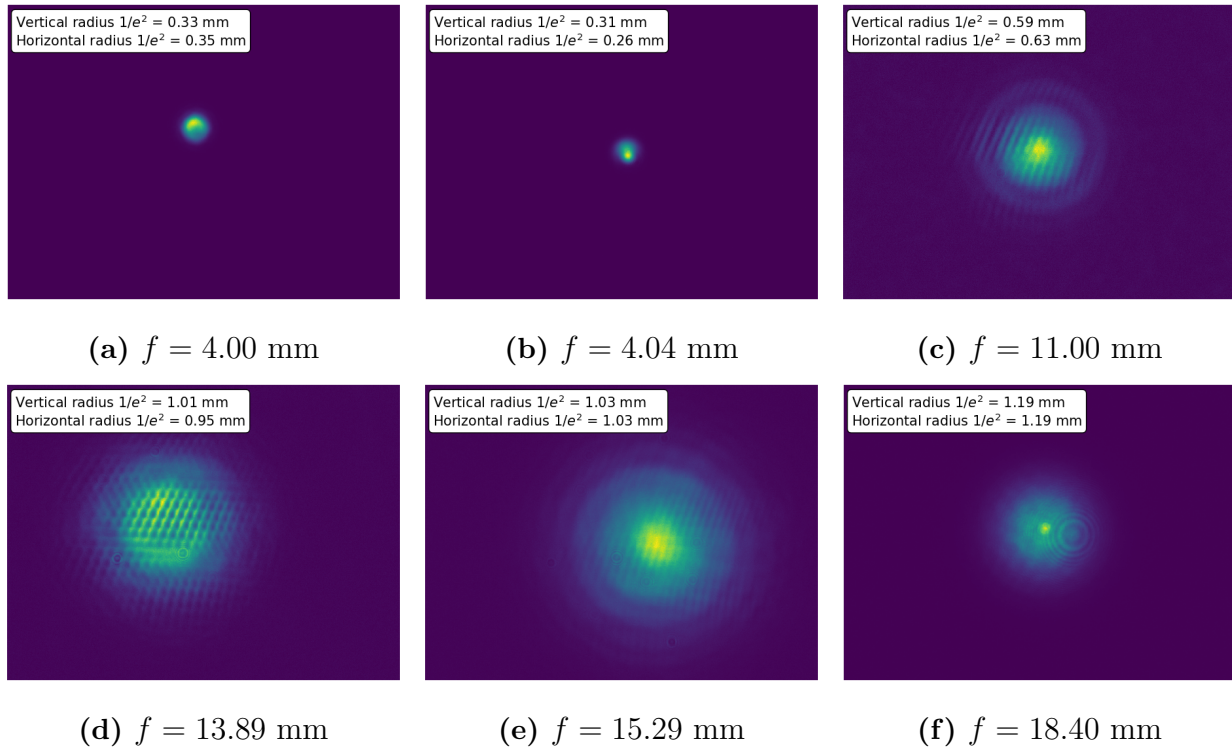

Figure 15: Images of beam outcoupled from fiber with different ashperic lenses. Figure **(a)**, **(b)** and **(f)** are taken with Lumunera camera. Figure **(c)**, **(d)** and **(e)** are taken with Unibrain camera. All pictures shows non-Gaussian behaviour.

- Collimation of beam, with different lenses, including imaging of beam shapes of collimated beams

3.2.2   Polarization stability

For the purpose of the transferring the control light from the laser table to the experiment a photonic crystal fiber[10] (PCF) was bought. The fiber is specifically designed for being able to handle high power, features a high transmission efficiency with polarization maintaining properties. This PCF was a prototype, since technological development in the field of fiber optics for many years mostly have been focus around red and infra-red wavelengths, as this is of great importance for the communications sector.

---

[10]NKT Photonics PCF PROTOTYPE
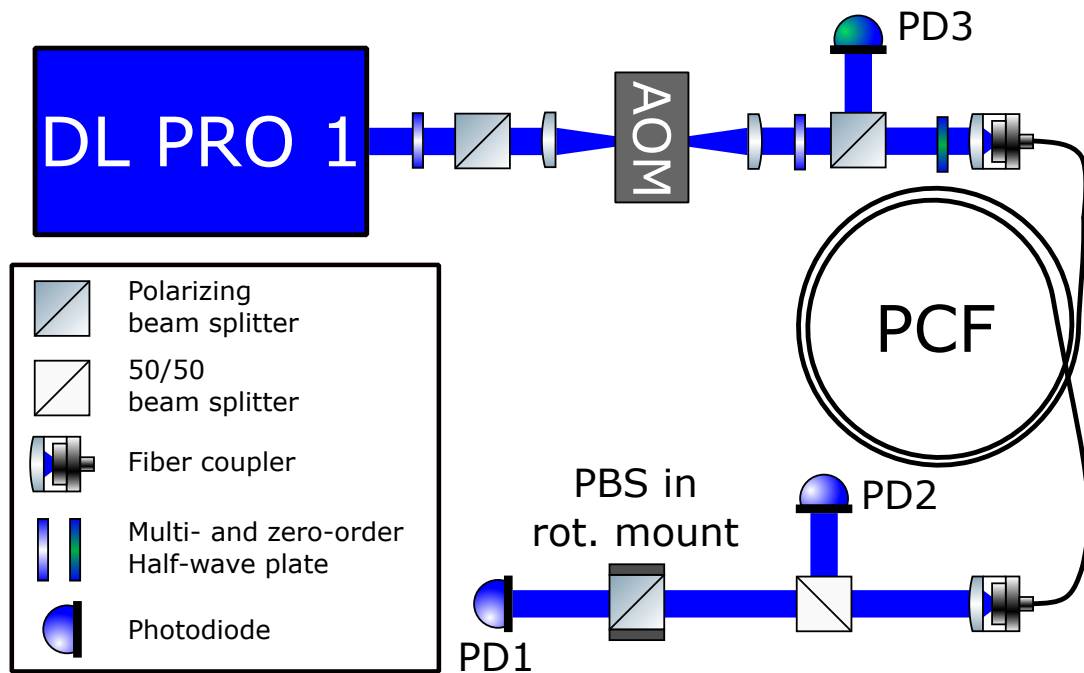
Figure 16: Polarization test setup for DL1.

For characterizing the polarization stability of the PCF the setup seen on figure 16 was put into place. As the control laser had some hardware issues with its Digital Laser Controller (DLC) at the beginning of testing, the DL 1 was used instead. The idea behind the setup, is to see on the photodiode behind the polarizing beam splitter (PBS) in rotating mount (PD1[11]) any there is any change in intensity on the diode over time. By rotating the PBS such that the minimum amount of light is transmitted, any polarization drift in the beam before the PBS should be apparent. If the signal changes, it would be impossible to determine if the drift is caused by an polarization drift or an intensity drift of the beam, since the PBS maps any polarization drift as an intensity drift, on only PD1. To make sure that it is polarization drift, a 50/50 beam splitter is put before the PBS in rotating mount. The reflected beam is detected on PD2[12], and will only see power drift, assuming the BS is not dependent on polarization. To make sure that any drift observed on PD1 and PD2 is caused by the PCF an additional photodiode[13] (PD3) is placed before the fiber. Any intensity drift from the laser will be detected on this photodiode.

All photodiodes are connected to a oscilloscope[14], which captures the data. The oscilloscope have 4 channels, and can contain 2000 data points per channel. The maximum time span the

---

[11]THORLABS DET100A2

[12]THORLABS DET100A2

[13]THORLABS DET10A2

[14]OSCILLOSCOPE NAME??

oscilloscope can capture over is 500 seconds. After capturing the data, it was transferred to a computer for analysis.

To couple into the PCF and collimating the beam after the PCF, two fibercouplers were built, respectively with lens **??** (f=**??**mm) and lens **??** (f=**??**mm). A zero-order half-wave plate (ZO-HWP) was placed in front of the polarization, to allow for matching the incoming polarization to the right axis of the fiber. According to manufactures specification, the linear polarized light should hit the fast axis of the fiber. To get an indication of the influence the incoming polarization has on the PCF, some preliminary measurements of the transmitted power when rotating the ZO-HWP was taken with a power meter. It had previously been seen determined that the PER of this ZO-HWP were better than 32.9 dB. The result of rotating the ZO-HWP 360° is sketched on figure 17. What is seen is a strange four fold symmetry, which were not expected.
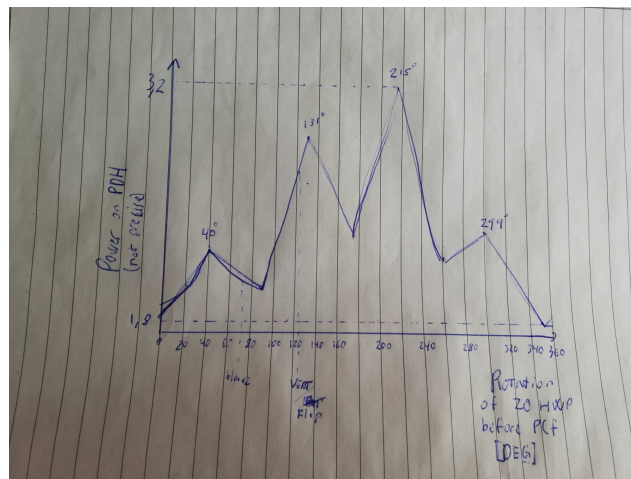
Figure 17: Polarization transmission with ZO-HWP??.

It was expected to have maxima of the same value and minima of the same value. To rule out that the effect was from a spatial deflected coming from the beam, the HWP was carefully moved on the table, and slightly angled to see if this were affecting the transmission. This was not the case. When another ZO-HWP, fresh from the box, was placed instead, the same effect was seen. However, the MO-HWP did not seem to have this behaviour. Since the maximum transmission of the ZO-HWP was better than the MO-HWP, it was decided to go on with the testing with the former HWP.

On the photodiode before the fiber (PD3), the power fluctuations of the laser was measured. It was seen, that the power were stable compared to the fluctuations seen on the photodiodes after the PCF. It will be omitted for brevity.

To find to optimal angle for the polarization going into the PCF is not trivial. By gently shaking the PCF to induce stress in it, it is clearly seen that at some angles, the fiber is much

more resilient to the disturbance. This procedure was done every time the angle was changed.

The first test was done by setting the ZO-HWP to 167°, which corresponds to the horizontal linear polarized coming from the PBS in front of the ZO-HWP, hits the fast axis of the PCF. The coupling efficiency was measured to be 37.2%. The maximum and minimum transmission of the PBS in rot. mount after the fiber was measured, and the PER of the cube was found to be 23.0 dB.

The PBS in rot. mount was then rotated to give minimum transmission of the photodiode, and three set of data was taken in sequence. Since the limit of the oscilloscope, it was not possible to take a continuous dataset longer than 500 seconds. The result can be seen on figure 18.
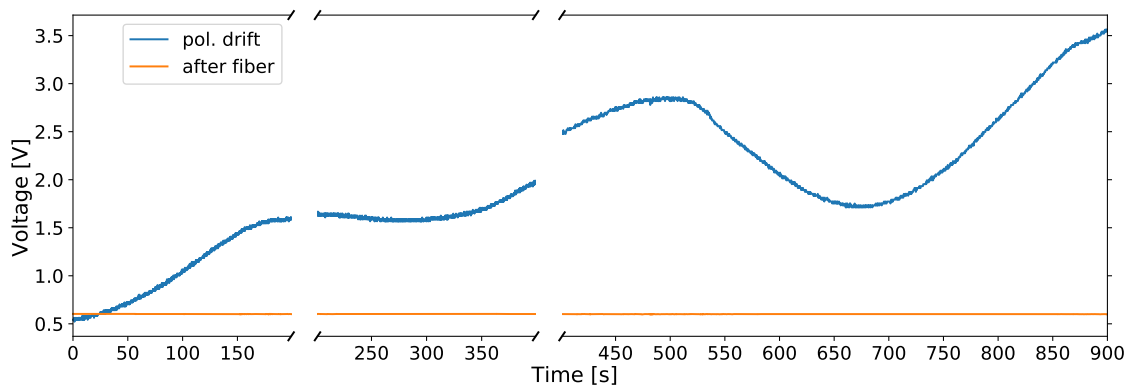
Figure 18: Set One - 167°.

The minimum signal from PD1 is assumed to correspond to the measured minimum intensity measured with the powermeter. The minimum signal is 0.522 V, and the maximum is 3.562 V. Assuming the intensity is proportional to the signal on the PD, it is possible to say that over the span of 900 seconds, the PER goes from 23.0 dB to 14.6 dB. As this can not be said to be very stable, is was deemed necessary to further examine if the optimal angle of the polarization in the incoupling had been chosen.

The next incoupling angle chosen was 212°, which corresponds to the highest transmission of the PCF. The coupling efficiency was measured to be 46.6% and the starting PER of the power meter was 30.3 dB. Same procedure as previously was done, and the result can be seen on figure 19.

The minimum signal over the span of 600 seconds were 0.10 V and the maximum 0.69 V. Assuming the minimum signal corresponds to the minimum intensity measured on the power meter, the PER spans from 30.3 dB to 22.0 dB. Again, very low stability as seen before, but with better PER overall.

Like shaking the fiber to find the angle where the fiber is most stable, it is possible to scan the laser to achieve the same effect. The transmission peak at 125° was chosen as the general
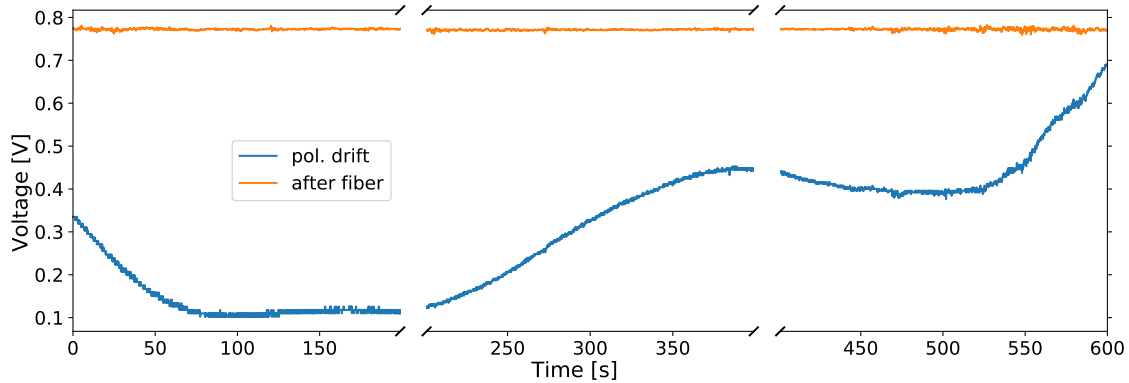
Figure 19: Set Two - 212°.

area to look in, and scanning the DL 1 with scan amplitude 5V at 10Hz, a coupling-angle of 121° found to be most stable. The measurements can be seen in figure 20.
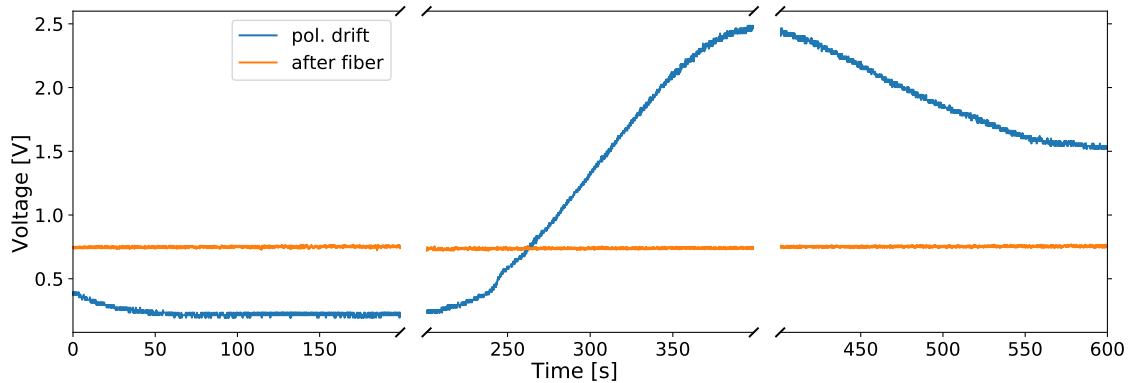

Figure 20: Set Three - 121°.

The chosen angle for the measurement in figure 20 is also not very polarization stable. The intensity of the minimum transmission of the PBS was not taken before starting the measurement. It is however possible to estimate the relative PER change to be around 12 dB, from the minimum and maximum of the signal.

During the time working with the polarization, some peculiar behaviour was observed. When changing the rotation of the PBS in front of PD1 after some drift had taken place, it was often possible to go down to the previous minimum found at the given coupling angle. This would mean that it is the polarization angle itself coming out of the fiber that had changed. Sometimes however, it would not be possible to achieve further extinction of the the beam with the PBS, meaning that at these times, it was not the polarization that had drifted, but rather the polarization extinction ratio.

As another PCF of the same type already had been returned to the manufacturer because of bad polarization stability, it was concluded that this type of fiber were simply not suitable for our purpose. This PCF was however not returned before it was found out, that it maybe was

the polarization optics that were the problem, and not the PCF. This is discussed in chapter 4.3.

4 Spot size imaging

Characterizing the focus of the probe beam is of crucial importance. Both the spot size of the focus, as well as the shape of the focus is necessary to know to a high precision. For this purpose, I have been spending a large amount of my time with developing ways to precisely characterize the spot size of the focused probe beam.

Script Introduction

All data analysis have been done with *Python* 3.7. The main script is based on work done by former group member Dr. Simon Ball. It has been heavily modified since the start of this thesis.

The primary function of the script is to load one or more images of a beam. For each image the horizontal and vertical beam waist is calculated and shown. This is done by summing all the rows of an image into one array, and then fitting a Gaussian function to said array. This is likewise done for all columns to find the vertical size of the beam.

Fitting a Gaussian is done by Scipy library's *curve_fit* function. This function fits any defined function, in this case a Gaussian, to the a given data set. It then returns the optimal fit parameters by using the least square method. The fitted parameters together with the pixel size (and when necessary, magnification) of the camera then gives the size of the two axes of the beam. The main parameter for beam characterization is the width of the Gaussian, which is converted into the $1/e^2$ radius of beam, being the most common way of describing Gaussian beams.

In the latest version the functionality has been further expanded. The script can now automatically estimate the position and size of the imaged beam. From these estimates, the script crops each image, and then the row and column summations are performed. The script plots the summation arrays, and the fitted Gaussians. Furthermore, if the images have been taken at different transversal positions, the divergence of the Gaussian beam (see chapter 1.4.1) is fitted with *curve_fit* and plotted for the waist of the images.

4.1 Lumenera Lt365RM

Two Lumenera Lt365RM was bought for the purpose of absorption imaging, but since they were not needed for the experiment at the time the spot size characterization was done, it was deemed a good idea to use this camera for spot size characterization, mainly due to its relative low pixel size (4.54um x 4.54um), compared to other cameras available, e.i. the Unibrain Fire-i 530b camera with pixel size 7.40um x 7.40um.

4.1.1   Image acquisition

Images were acquired with the *LuCam Capture, version 6.8.2.* This simple interface controls the camera via USB 3.0, and allows for setting the exposure time of the camera. The video of the camera was used as a preview of the beam, with the actual images being taken as a snapshot with a set exposure, and the shown picture can then be saved as a 14 bit TIF image [**LuCamSpecs**].

4.1.2   Microscope Design and Characterization

Since the expected spot size of the probe beam was around 6 um, focusing the beam on the camera sensor would result in a three pixel wide signal. This was judged to be too small a data set to reliable fit a Gaussian to, so a plan of enlarging the spot was made.

As describe is chapter 1.4.2, a microscope requires both an objective and a tube lens/eyepiece. The availability of a high performance microscope objective[15] lead to the design of the microscope shown in figure 21. A 200 mm focal length plano-convex lens[16] was chosen as the "eyepiece". The focal length is a compromise between high magnification, and to not have the assemble microscope to be too unwieldy. This lead to a microscope with magnification of around 20x, which would mean that a spot 3 pixels wide directly on the sensor, should be 60 pixels wide with the microscope.
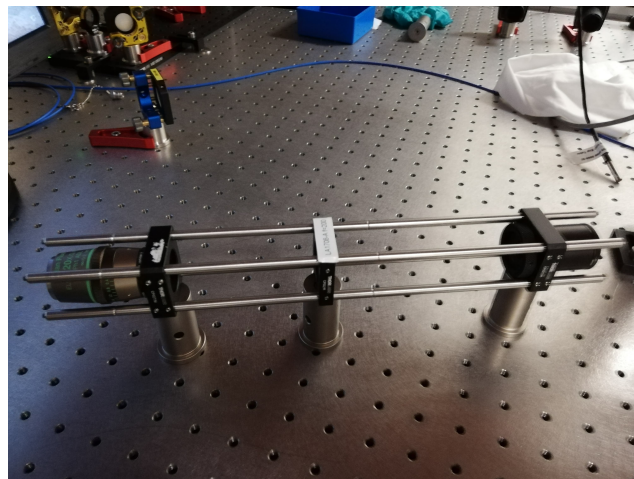
Figure 21: Picture of microscope. Lumenera camera not attached.

For determining the spot size of the probe beam, precisely knowing the magnification of the microscope is necessary. For this a USAF 1951 target (see figure 22) is used. This is a standardized method of measuring optical performance. The USAF 1951 target consist of

---

[15]Nikon Plan Flour 20x
[16]Thorlabs LA1708-A

multiple line pairs, where each line pair has a group number and an element number. The resolution of each line pair is given by

$$\text{Resolution [lp/mm]} = 2^{\text{Group}+(\text{Element}-1)/6} \tag{4.1}$$
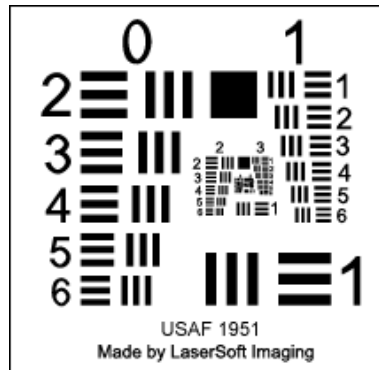

**Figure 22:** SilverFast USAF 1951 Resolution Target [82].

By imaging a known line pair with the microscope, it is then possible the find the magnification of the microscope. The test target furthermore gives an indication of how small an object the microscope can image.

When imaging the test target, it was quickly seen that the coherence of the laser light coming from DL PRO 1, was severely decreasing the resolution of the imaging system, see figure 23a. Two methods of making the laser light incoherent was used.

First method was by reducing the laser diode current to below the lasing threshold. At low current the laser diode behaves as an LED. The current was reduced from 38.65mA to 20.65 mA, well below the lasing threshold according the lasers specifications [**TopticaDLProManual**]. A somewhat sharper image was obtained. The image obtained can be seen on figure 23b.

Second method was using a home-made diffuser. It has been made by gluing a round piece of wax paper, on a computer fan with the fan blades removed. The rotation of the diffuser figure makes sure, that any unevenness of the diffuser, will not be shown on the final picture. The image obtained can be seen on figure 23c.

Finally, taken by using an ordinary flash light which can be seen on figure 23d. Using a flash light will guarantee that the light is not coherent, but will have a chance of making the image resolution worse, because of the introduction of light at a higher and broader spectrum wavelength than 399 nm.
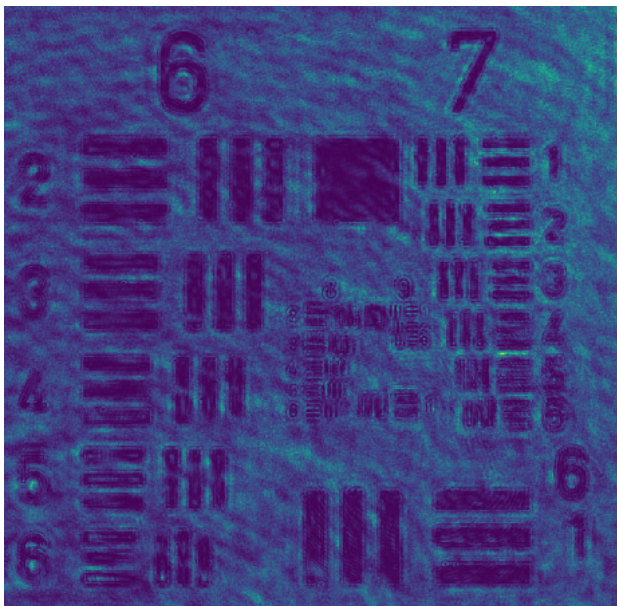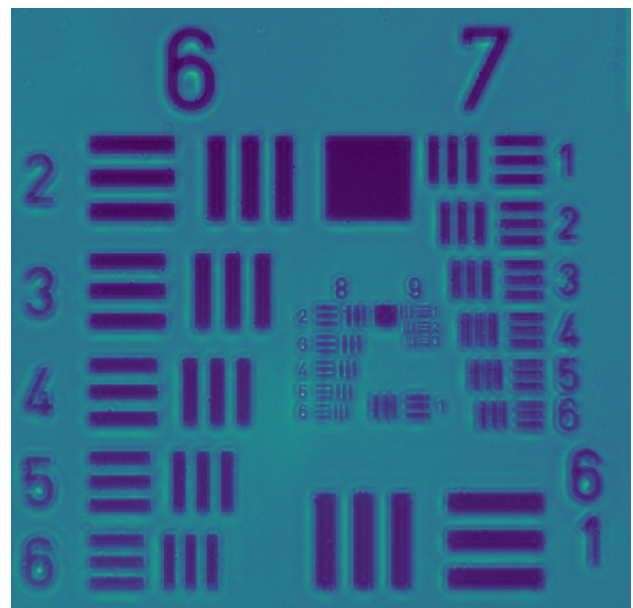
(a) Laser directly on test target
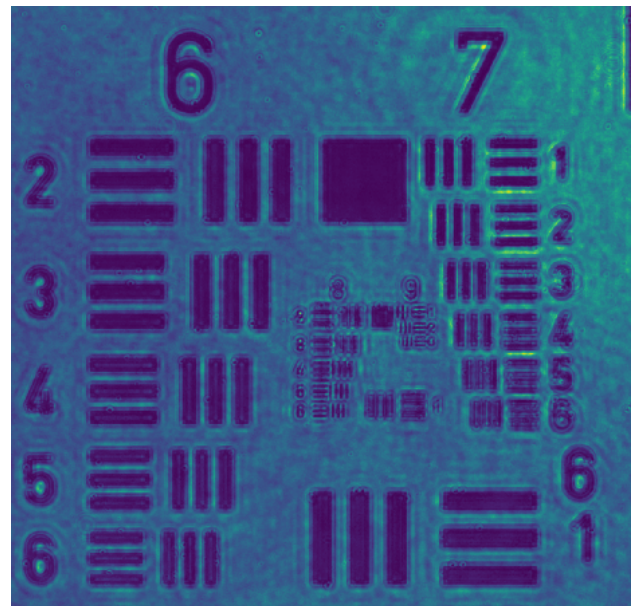
(b) Laser, below lasing threshold, laser diode current 20.65 mA.
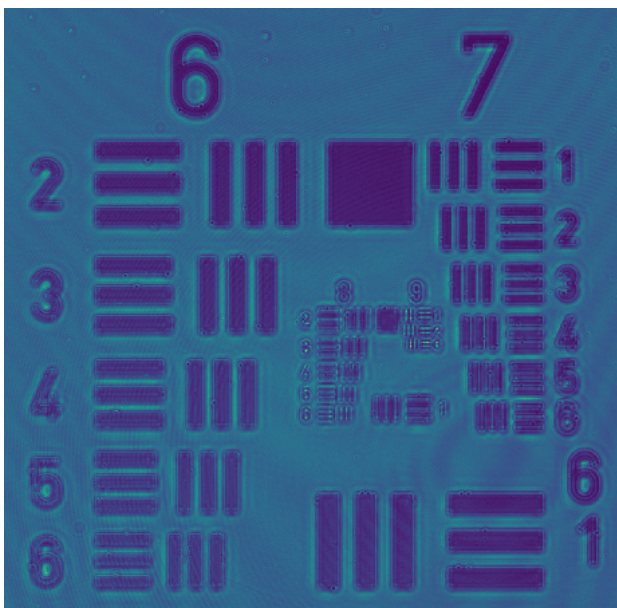
(c) Laser, with diffuser

(d) Flash light

Figure 23: Pictures of USAF 1951 test target with different light source. All pictures cut and rotated counter-clockwise by 90 degrees. Line pair from group 6 element 1 to group 9 element 3 present.

To find the size of a given line pair on the image, an area of interest is drawn around said line pair. For vertical lines all rows in the area of interest is summed into a single array. Likewise for horizontal lines all columns are summed into an array. A sine wave function is

then fitted on the arrays with the *curve_fit* function in Python. The frequency of this sine times the pixelsize then corresponds to the imaged size of the line pair, which can then be divided by the size found with equation 4.1 to find the magnification of the line pair. A sine wave was chosen, as it is a simple function, which is easy to fit for the *curve_fit* function.

From figure 23, it was decided that the best looking image, was the one taken with a flash light as light source. Finding the magnification of all elements of group 6 and group 7, and averaging the magnification for each line pair, gives 19.48 ± 0.33 for the vertical lines, and 19.42 ± 0.52 for vertical lines.
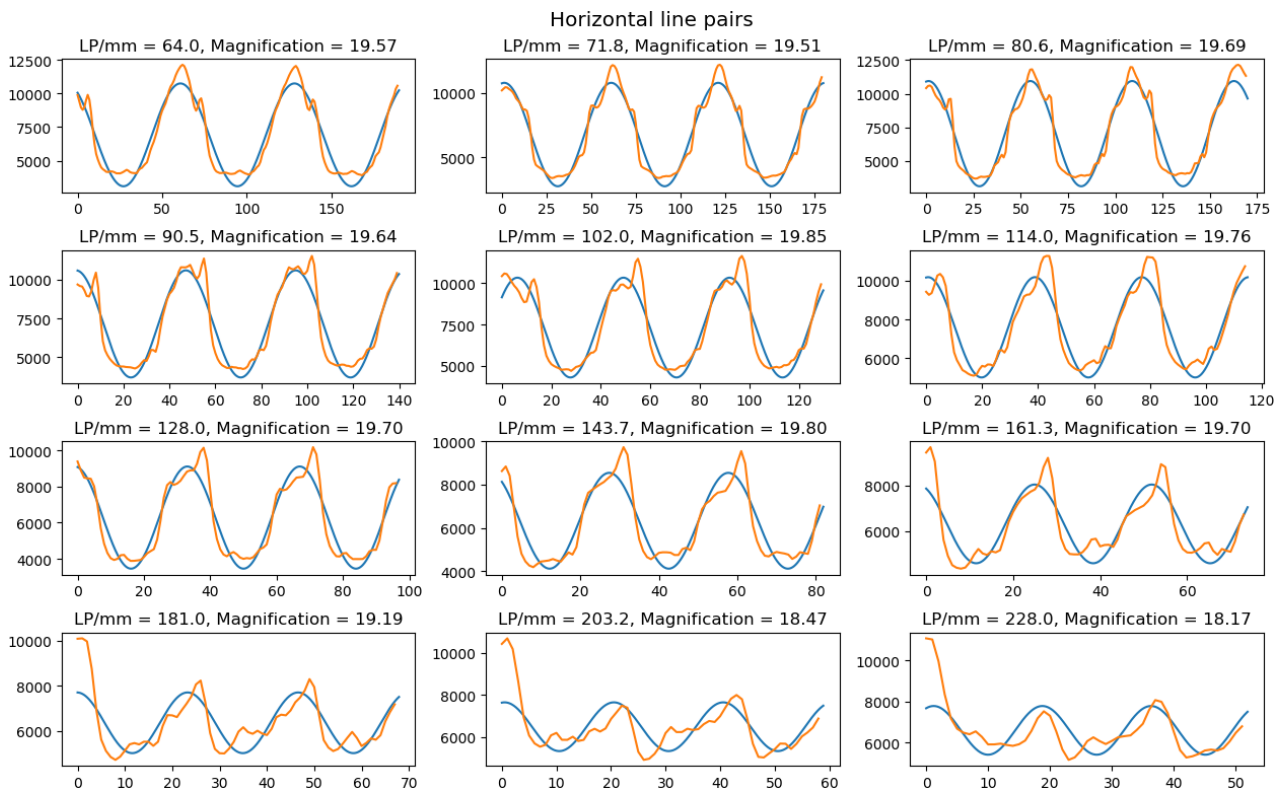
Figure 24: Test target Horizontal, group 6 and group 7. Average magnification 19.42 ± 0.52. Similar results obtained from the vertical line pairs.

From the fits in figure 24, it is easily seen, that as the line pairs gets smaller, the signal to noise ratio, and thereby the accuracy of the fits, decreases. Together with the fact that the size of the array the sine wave its fitted on also gets smaller with smaller line pairs, makes the calculated magnification more and more sensitive of errors in the period of the fitted sine wave the smaller the line pairs is. From that, it is concluded that the most trustworthy magnification is found with the sine wave of the largest line pairs.

To get a feeling if a focused beam, with spot size of around 5 µm is resolvable with the microscope, the smallest line pairs on the test target was examined. Four line pairs was chosen: Group 8 element 1 with line width 1.95 µm, Group 8 element 6 with line width 1.10
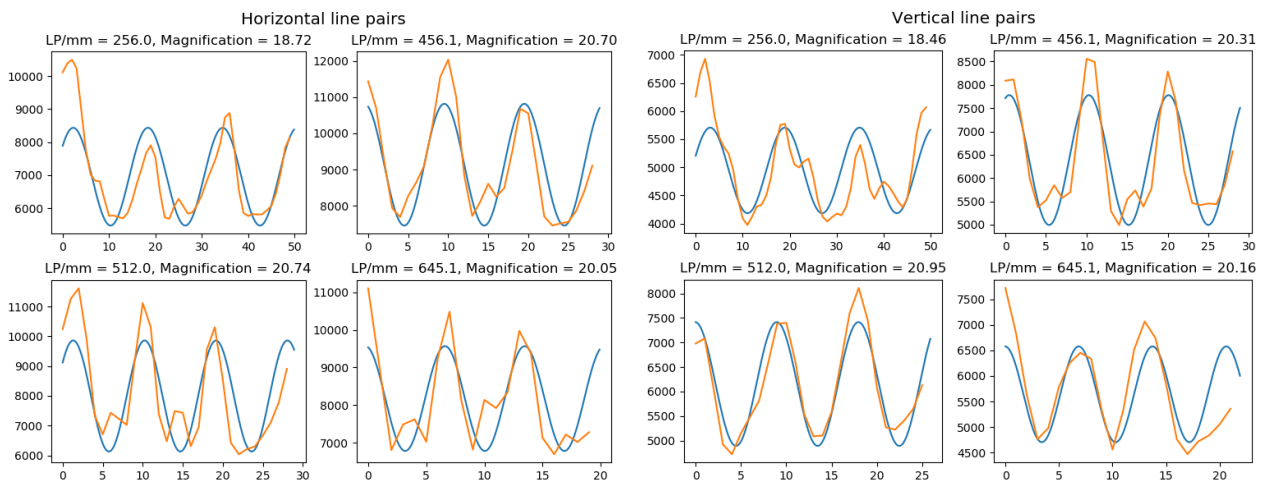
µm, Group 9 element 1 with line width 0.98 µm and Group 9 element 3 with line width 0.78 µm.
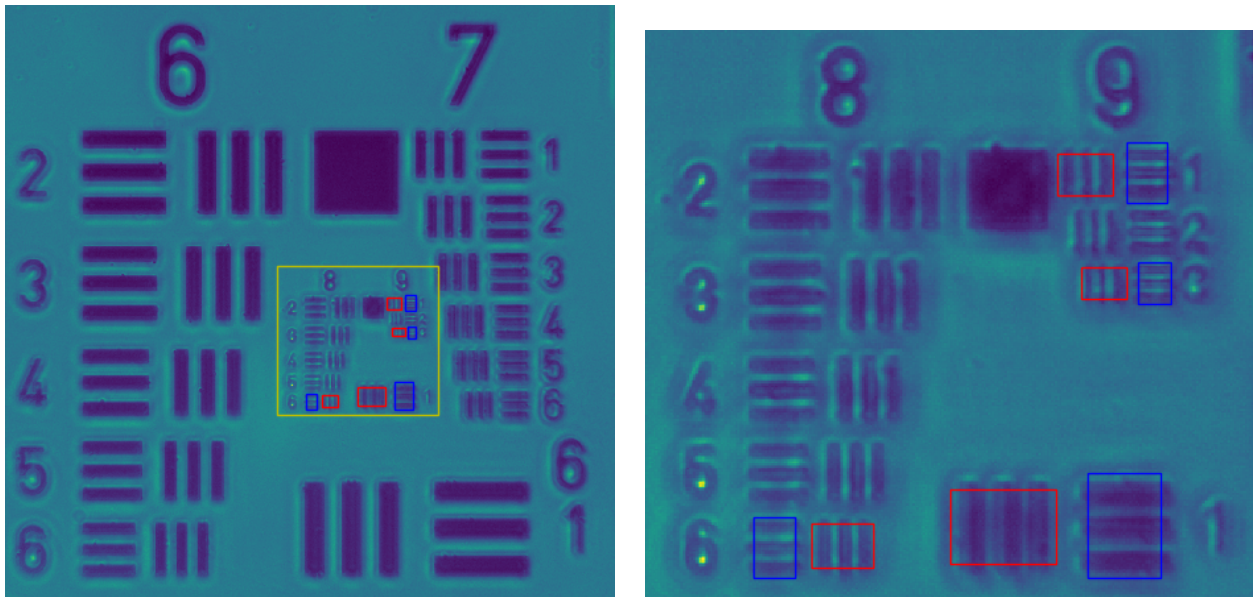
(a) Shows the position of the smaller groups.

(b) Group 8 and group 9, zoomed in.

Figure 25: The area of interested of the two small groups.

(a) Horizontal line pairs.

(b) Vertical line pairs.

Figure 26: The line pairs: Group 8 element 1, Group 8 element 6, Group 9 element 1 and Group 9 element 3.

As seen of figure 26, the small line pairs are still resolvable, which means that details in the focus spot as small as 0.8 um should be visible. The microscope fulfils our requirement, being able to image a spot size of 5 µm and spots down to 0.8 µm.

4.1.3 Spot Size of Probe

Finding the beam waist of a focused beam, Gaussian optics dictates that beside imaging the spot itself, it is possible to calculate the beam waist from the divergence of the beam. This was done on figure 27, without any optics other than the outcoupler and probe lens. This method however doesn't give any information about the mode of the spot in the near field. The camera was moved 5 mm closer to the probe lens for each image taken.
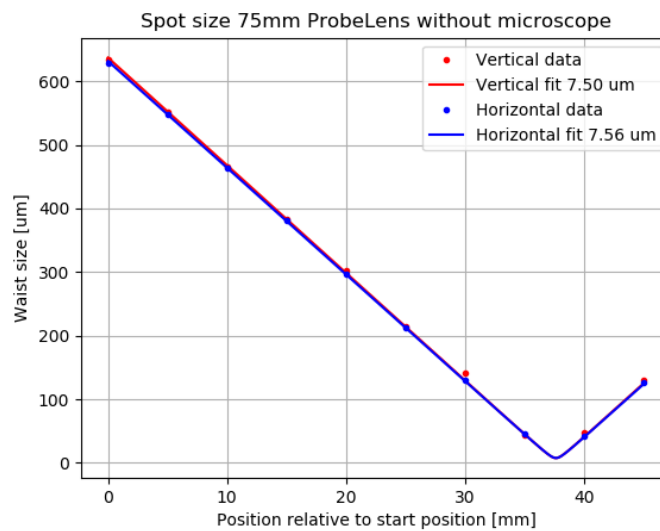

Figure 27: FarField without microscope.

The setup seen in figure 28 was put in place for imaging the focused probe beam with the use of a 75 mm focal length achromatic cemented doublet lens[17]. Three micrometer translation stages[18] was combined to allow of three dimensional movement of the probe lens, which was mounted in a kinematic mount[19] to tilt and pitch the probe lens. The three dimensional translation stage was then mounted on top of yet another translation stage, to expand the range of motion in the coaxial direction of the beam. This setup allows for 25 mm translation on the horizontal and vertical axes perpendicular to the beam, and 50 mm travel along the beam. All four translation stages had engraving every 10 um and resolution being 500 µm translation per revolution.

The expected $1/e^2$ spot size is: $w_f = \frac{\lambda f}{\pi w_0} \rightarrow w_f = \frac{399\text{nm} 75\text{µm}}{\pi 1.25\text{µm}} = 7.62\text{µm}$

Since the microscope was too unwieldy to mount on a translation stage, the probe lens and outcoupler is instead mounted of the translation stage, and moved away from microscope between each image. On figure 28 the beam waist around the focused beam can be seen.

---

[17]Thorlabs AC127-075-A
[18]THORLABS, PT1/M, Single-Axis Translation Stage with Standard Micrometer
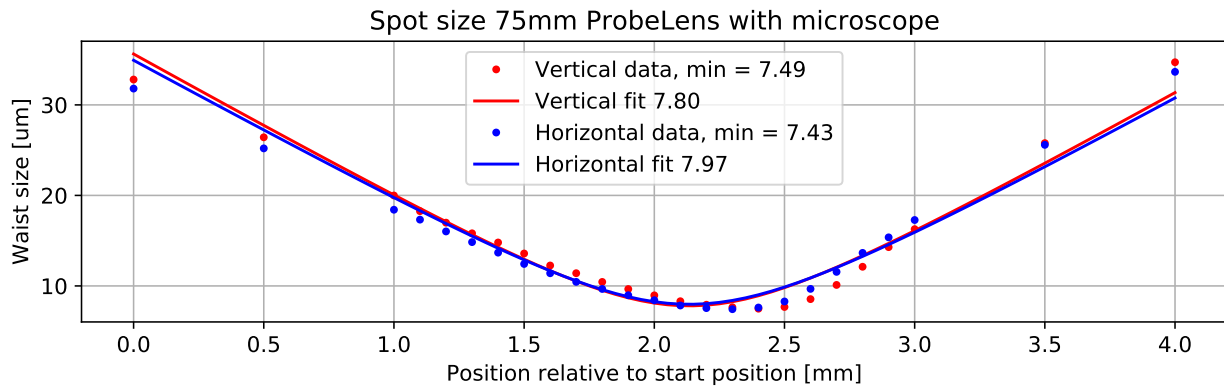[19]KINEMATIC MIRROR MOUNT

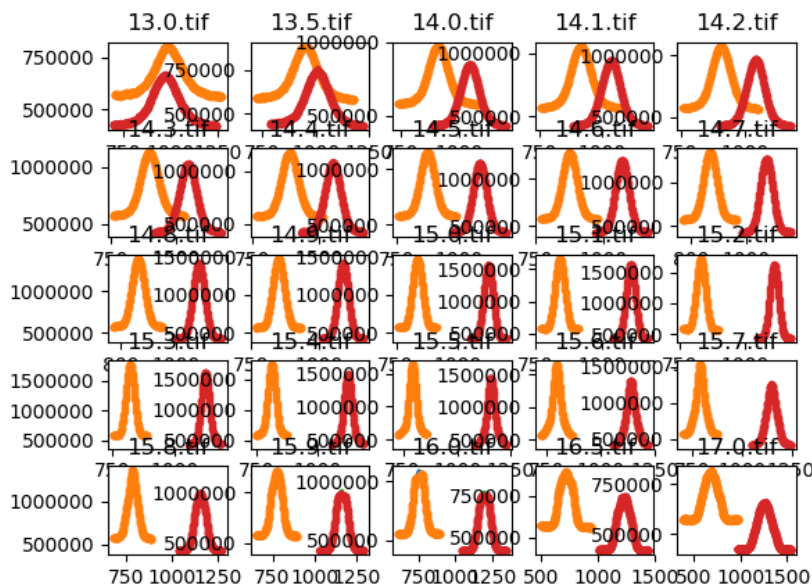**Figure 28:** Spot size 75mm ProbeLens with microscope.

Figure 29: Spot size 75mm ProbeLens with microscope - Gaussian fits.

The fitted beam of both the horizontal and vertical fits are seen to not follow the data points very well around the focus of the beam. The beam seem to be diverging out significantly weaker after the focus, than it is focusing. By looking at each picture in figure 30, it becomes clear that some unwanted behaviour is present at the pictures from 2.5 mm and further away. Before this point, the beam seems to be nicely Gaussian. Possible reasons for this unwanted behaviour could be:

- **Non-Gaussian beam** - The beam being focused is not the fundamental transverse Gaussian mode. If this is the case, then both the Gaussian fitting to each picture, and the beam divergence of the found waists no longer hold true. This would also be a huge

problem if it is implemented into the final setup, as the probing of the Ytterbium cloud is very dependent on a clean fundamental Gaussian mode. This issue should be able to confirm or deny, by closely examining the beam profile of each picture close to the beam waist.

- **Microscope** - It is entirely possible that the unwanted behaviour is not the beam itself that is not propagating nicely, but that the microscope introduces some aberration of the beam. Since the front surface of the objective is in the focus of the beam, but rather the objectives focus length away, the imaging cannot be said to be truly of the near field of the spot. To see if is the fact that the microscope is in fact not imaging the spot itself, but rather the projected far field, some tries of measuring the beam focused on/through a surface was tried.

- **Measurement** - Since the precision of the translation stages are significantly higher than the distance between each picture, and was adjusted carefully with every image taken, it is very unlikely that the inconsistency between the fit and the data seen on figure **??** is due to measurement reading mistakes. The Gaussian fits giving the spot size for each image can be see on figure **??** and show high agreement between the Gaussian and the data points, which indicates that the fitting method is not at fault for the strange behaviour.

To see where this behaviour stems from different methods where used, which can be see in the following sections. The beam was focused on/through different objects, with the idea that imaging scattering light would better preserve the size and shape of the focus. Another lens was also used, to see if the behaviour is dependent on the chosen probe lens.

Diffusers

The purpose of using a diffuser, was to eliminate the possibility that the non-Gaussian behaviour was an effect of the far field imaging. As a proper diffuser was not available at the start of the investigation, different alternatives was consider.

On figure 31 the different "alternative" diffusers are shown. Two paper types was shone through, but as seen, the first type (Thorlabs Post-It) was so thick, that sever diffusion of the beam happened, making the beam appear way larger than it actually was. The second paper type (Thorlabs lens tissue), while thinner than the Post-It type, but had too large fibers, making analysis of the beam almost impossible. The third idea was to look at the trace amount of light coming out of the backside of a mirror when shone upon by the beam. The very low transmission of the mirror however prevents a high enough light intensity, to get a good signal to noise ratio.
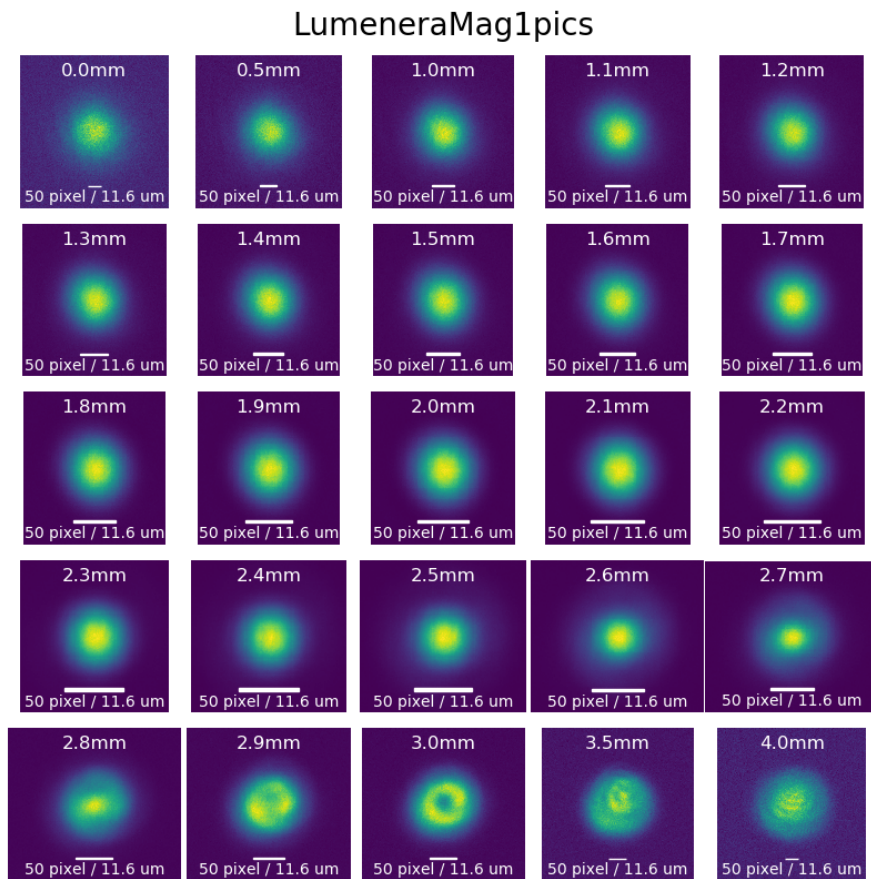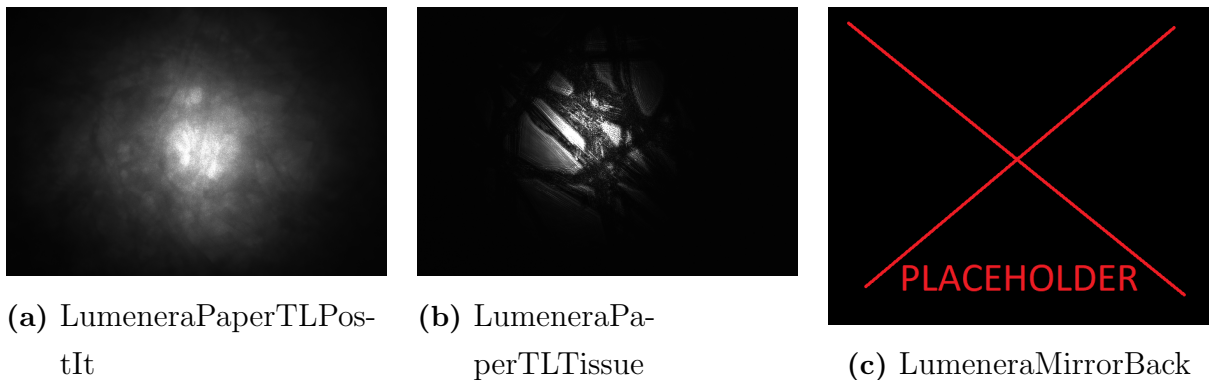
Figure 30: LumeneraMag1pics.

(a) LumeneraPaperTLPostIt

(b) LumeneraPaperTLTissue

(c) LumeneraMirrorBack

Figure 31: LumeneraDiffuser.

After determining that the tried objects was not useful, a diffuser[20] was acquired. Focusing the beam on diffuser, the coarse surface was placed towards the probe lens, and the camera placed behind the diffuser. The spot size at different positions close to the focus spot was taken as before. The result can be seen on figure 32a.

Again, the same characteristics of the beam waist can be seen. No apparent deformation

---

[20]TL DG05-1500
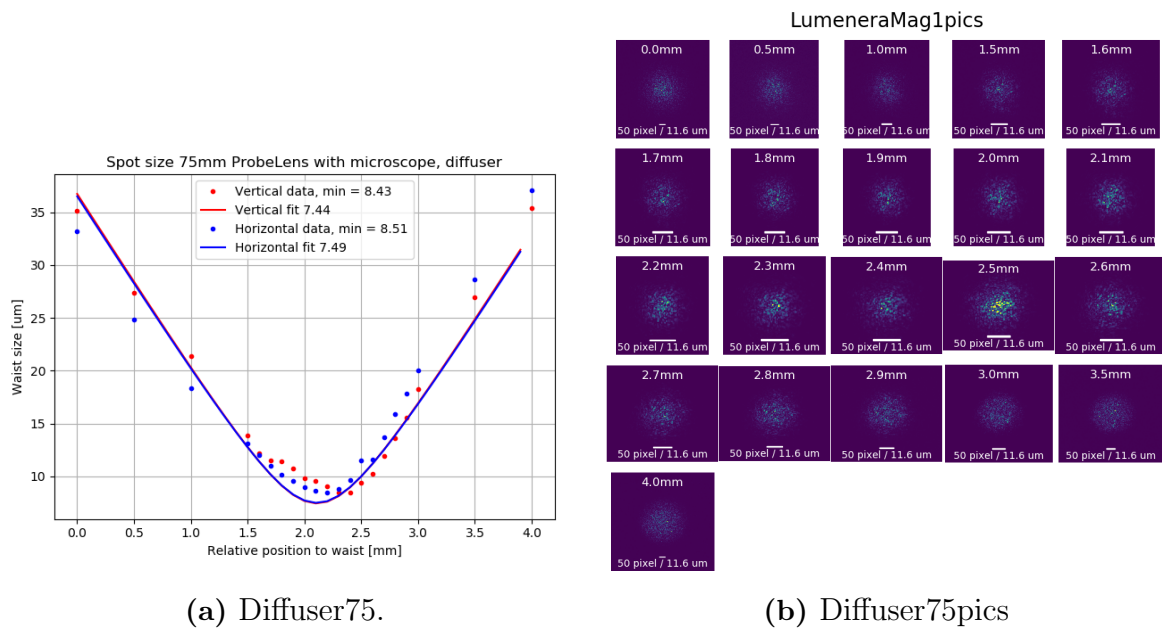
(a) Diffuser75.

(b) Diffuser75pics

Figure 32: LumeneraDiffuser.

of the beam if any of the images in figure 32b. However, this is hard to determine for sure, due to the image quality. The found beam waist from the divergence, 7.44 um x 7.49 um, corresponds nicely with the previously found values. The lowest fitted values are however 1 um higher than the fitted values. This is a first indication, that the fit of the divergence might not be very good. The size increase might be caused by light diffusing on the surface of the diffuser, and/or the fact that the light have to propagate through the glass, and out of the backside of the diffuser to reach the camera.

A second test was done by putting the coarse side in the microscopes focal point, and then hitting this surface with the beam, at an angle. The way the microscope is constructed puts constrains on both how close the probe lens can get to the diffuser, and at what angle the diffuser are to the beam. On figure 33 the setup can be seen, with a drawn on guides. With this a rough estimate of the incident angle of the beam on the diffuser are found to been around 71°.

The same set of measurement are taken as previously, and the results in figure 34 are obtained. The vertical waist found for each image, have all been multiplied by cos(71°), to compensate for the fact that the apparent size of the beam on the diffuser, is at projection of the actual beam size.

Figure 34a clearly shows that some issues arises with the used method. Looking around the focus of the beam (position 12 mm), it is seen, that the angle correction is approximately correct, as the vertical and horizontal data point are well aligned. At a distance away from the focus, the vertical and horizontal evolves very differently. This could be explained by
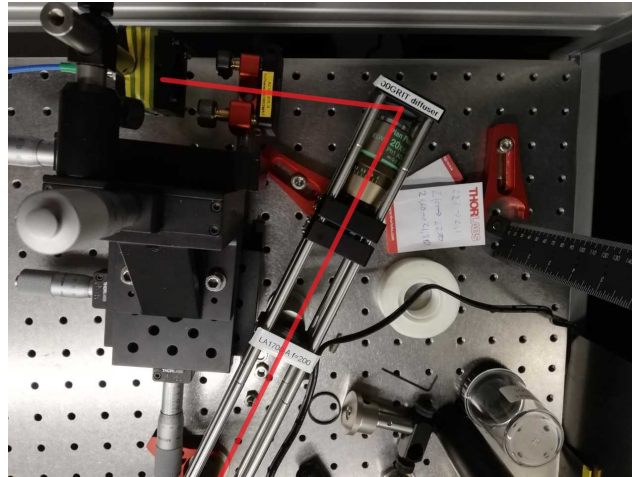
Figure 33: DiffuserAngle
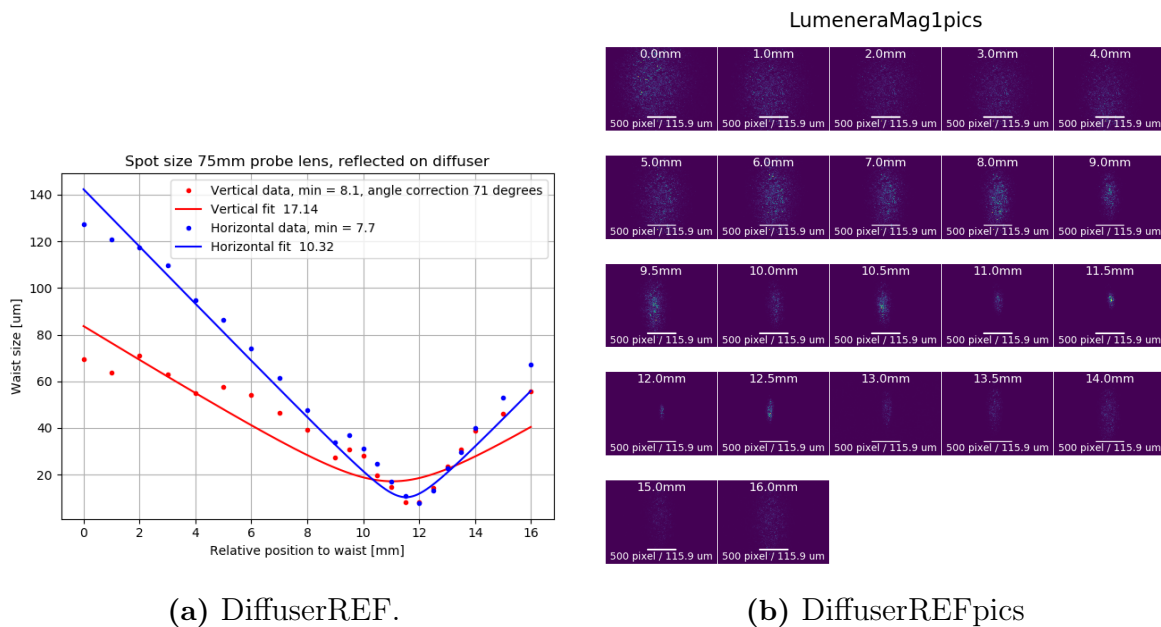

(a) DiffuserREF.

(b) DiffuserREFpics

Figure 34: DiffuserReflected.

at change in incident angle of the beam, as the probe lens is moved. However, this is very unlikely, as both the translation stage on which the camera and the microscope, were firmly secured to the optical table.

The method used with the scattered light from the diffuser is also very noisy for the fitting script to process, as seen on figure 35. As a result, it is very unclear from both images and their fits, if the dark spot, as observed on figure 30, is still present.
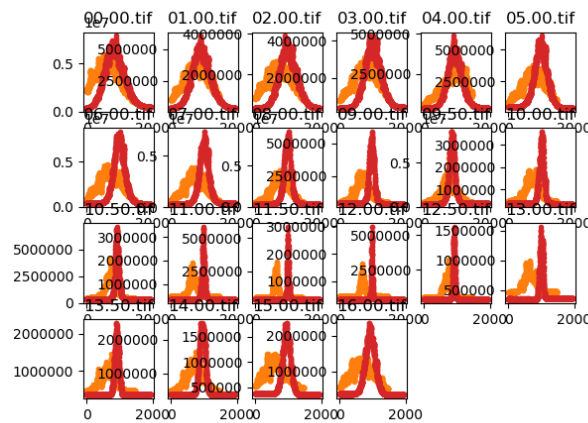
Figure 35: DiffuserREFfits.

4.1.4   New lens (19 mm achromatic cemented doublet)

As the issues observed could be connected to the probe lens, and not the microscope, another lens was tried. A 19 mm focal length achromatic cemented doublet[21] was chosen as it was the only other cemented doublet available at the time. The expected $1/e^2$ spot size is 1.93 um, which is still resolvable as shown previously.

All the same measurements as for the 75 mm probe lens was done. First the far field measurement, to get an idea of the actual spot size.
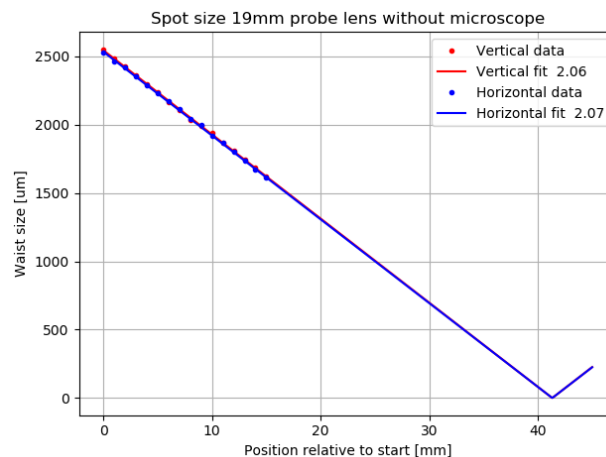

Figure 36: Far field for 19mm probe lens.

The spot size at is a bit larger than expected, but well within the expected limits.

On figure 37, the beam waist around the focus is seen. Figure 37b is zoomed in version of figure 37a. The found spot size corresponds nicely with the spot size found from the far field.

---

[21]Thorlabs: AC127-019-A

As with the 75 mm lens used in the previous section, the beam is focusing more strongly than it is diverging, which should not be the case for a purely Gaussian beam. The behaviour around the focus (1.3mm to 1.5mm) have not previously been seen.
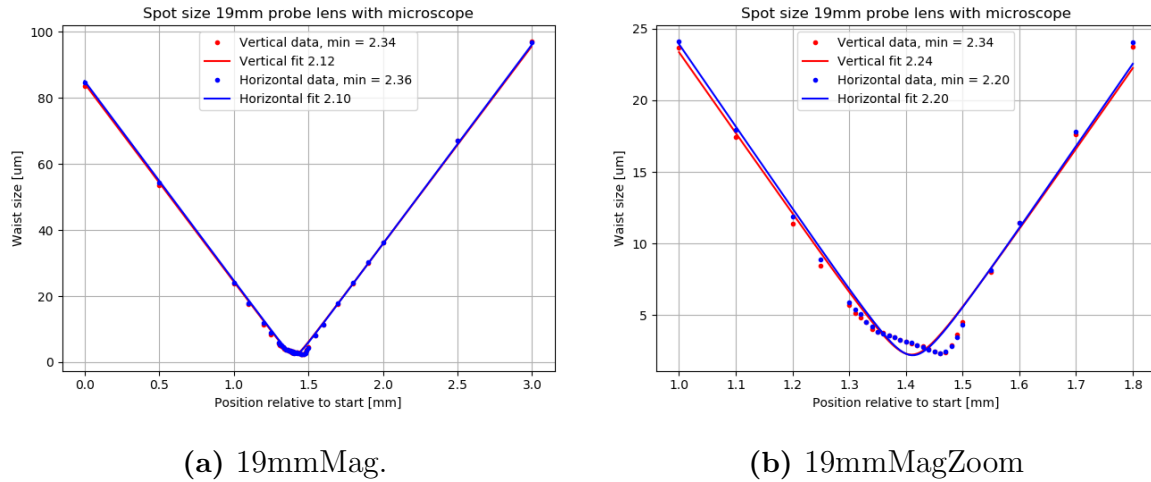

(a) 19mmMag.

(b) 19mmMagZoom

Figure 37: 19mmMagnification.

By looking at the images of the beam on figure 38, it quickly becomes clear that the beam is not Gaussian. A very clear circular diffraction pattern is present both before and after the focus. This is the most likely cause that the beam is not single mode.

As with the 75 mm lens, the measurement was also done with a diffuser, which can be seen on figure 39. Again it is clearly seen, that the focus of the beam is not diverging as a Gaussian beam, similar to without a diffuser. However, the "stretching" out of the focus is not as predominant as before. The minimum waist is a bit higher, than when not using a diffuser. This effect was also seen with the 75 mm lens, and is possibly cause by the diffusing of the light.

The cause of this behaviour, and of the similarities and difference to the images taken without the diffuser, doesn't become more clear by looking at the images of the beam without the diffuser in place. Because of the scattering effect, it is not clear if any diffraction pattern is present.

4.1.5 Summary

With a Lumenera Lt365RM camera, the spot size and shape of a collimated beam focused by a potential probe lens candidate were examined. As the pixel size of the camera is too small to image the spot size of the focus, a optical system were constructed to magnify the spot, and more thoroughly examine the focus.

Both the far field calculation and the direct imaging of the proposed 75 mm probe lens
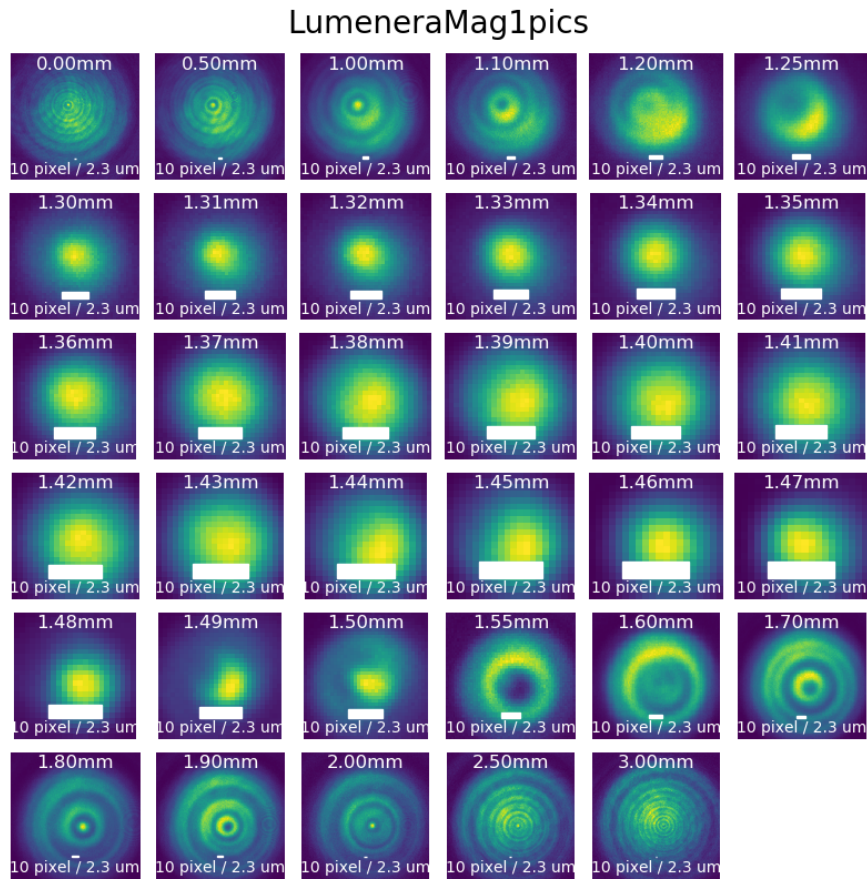
Figure 38: 19mm probe lens with magnification.
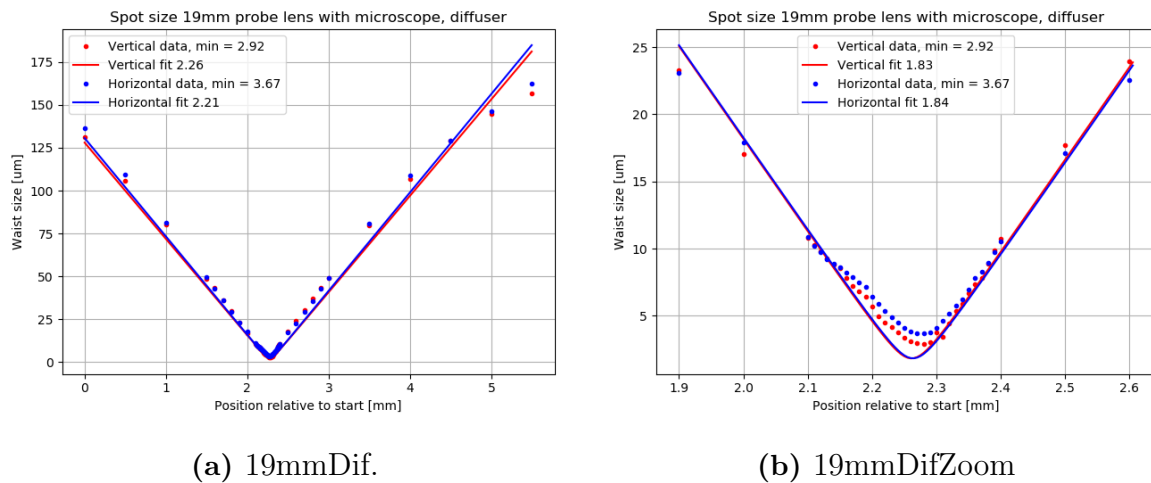

(a) 19mmDif.

(b) 19mmDifZoom

Figure 39: 19mmDiffuser.

confirmed the expected spot size at around 7.5 um. While the spot is as expected, the presence of a dark spot in the beam after the probe lens, but before the focus, together with the fact, that the beam is focusing stronger than it is diverging, brings the beam quality into question.

Using a diffuser to scatter the light of the focused beam, to rule out that effect was cause by some unknown properties of the imaging system, gave inconclusive results.

All test were also done with a different lens, which gave similar inconclusive results.

4.2 Raspberry Pi NoIR v2 Camera

Since the characterization of the probe beam focus, at best were inconclusive with the Lumenera camera, other alternatives were investigated. As discussed in chapter **??**, beam profiling can also be done with other methods, than imaging the beam itself. However, since none of these alternatives were not available, another try to image the spot size was made.

Previously a Raspberry Pi NoIR v2 camera had been used for characterization of all the lasers. Since the pixel size is significantly smaller than the other available cameras (1.12 x 1.12 um for the Raspi Cam, against 4.54 x 4.54 um for the Lumenera Lt365RM), it could potentially be used in directly imaging the focused spot, with no magnification. It was later found out, that without a lot of precaution, the quantitative information in the images were unreliable. Specifically, when using the camera to take pictures in the default capture mode, even when fixing all available options (such as contrast, white balancing and gain), some preprocessing of the image was done by the Raspberry Pi camera's on-board GPU. The effect of this, was that taking the same image with different exposure time, changed the apparent size of the beam. For this reason, the Raspberry Pi camera was dismissed as an option, when the characterization the probe beam was started.

After the beam characterization with the Lumenera camera proved unsuccessful, further investigation on the Raspberry Pi camera showed, that other optic groups have had same issues with the camera [**someGroup**], but was been able to bypass the preprocessing, and directly load the image from the camera as Bayer data. With assistance from Mohammad Noaman, a way to capture and analyse Bayer data taken from the camera was devised.

4.2.1 Image acquisition and analysis

The Raspberry Pi NoIR v2 camera has a Bayer filter CMOS sensor. Since a image where each pixel can be trusted as a relative intensity measurement, the raw output from the cameras sensor was needed. All interfacing with the camera was done with a *Raspberry Pi 3 model B+*, where each image were saved, and then transferred to a computer for further analysis.

The script for analysing the images are based on the same method as described in the previous chapter. The most significant difference stems from the fact that the pixels of the image has a Bayer pattern. This effectively means, that unlike the Lumenera camera, the read-out value of each pixels can not be compared to its closest four neighbour, the pixel and it's neighbours have different sensitivity to light at different wavelength. Having to treat each color of the Bayer pattern separately adds a additional layer of coding complexity, but fundamentally it does the same as the script describe in chapter **??**.

Only every second pixel for the green pattern are used, as it was observed that the the
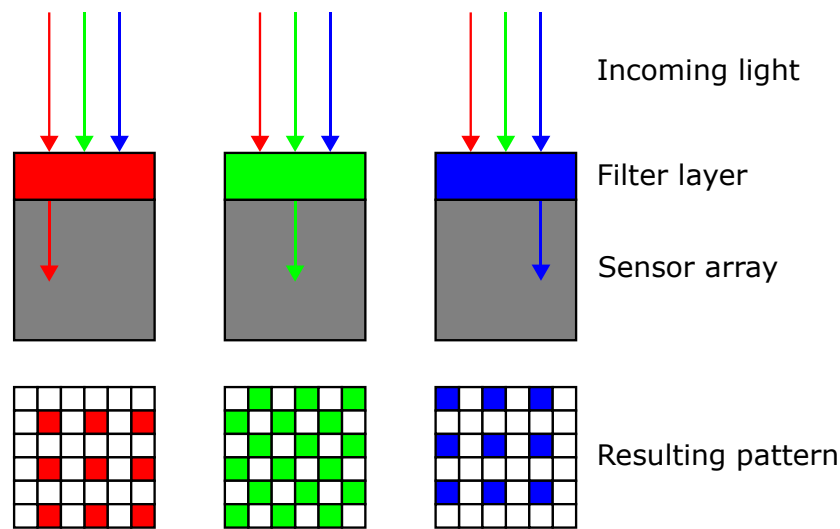
Figure 40: Bayer pattern on sensor [83].

read-out value for those pixel were significantly different from its four nearest neighbours.

4.2.2   Spot Size of Probe

As in the previous section, the spot size of the probe beam focused with the 75 mm achromatic cemented doublet lens was measured. On figure 41 the beam size as it is focused is shown. The start position of the camera is before the focus, e.i. near to probe lens, and then moves away from the probe lens as the position changes. The behaviour seen on figure **??** with the Lumenera camera, where the beam is apparently focusing sharper than it is diverging after the focus, is also present here. The found spot size for the different colors have small deviations from each other, but are within the expected uncertainty.
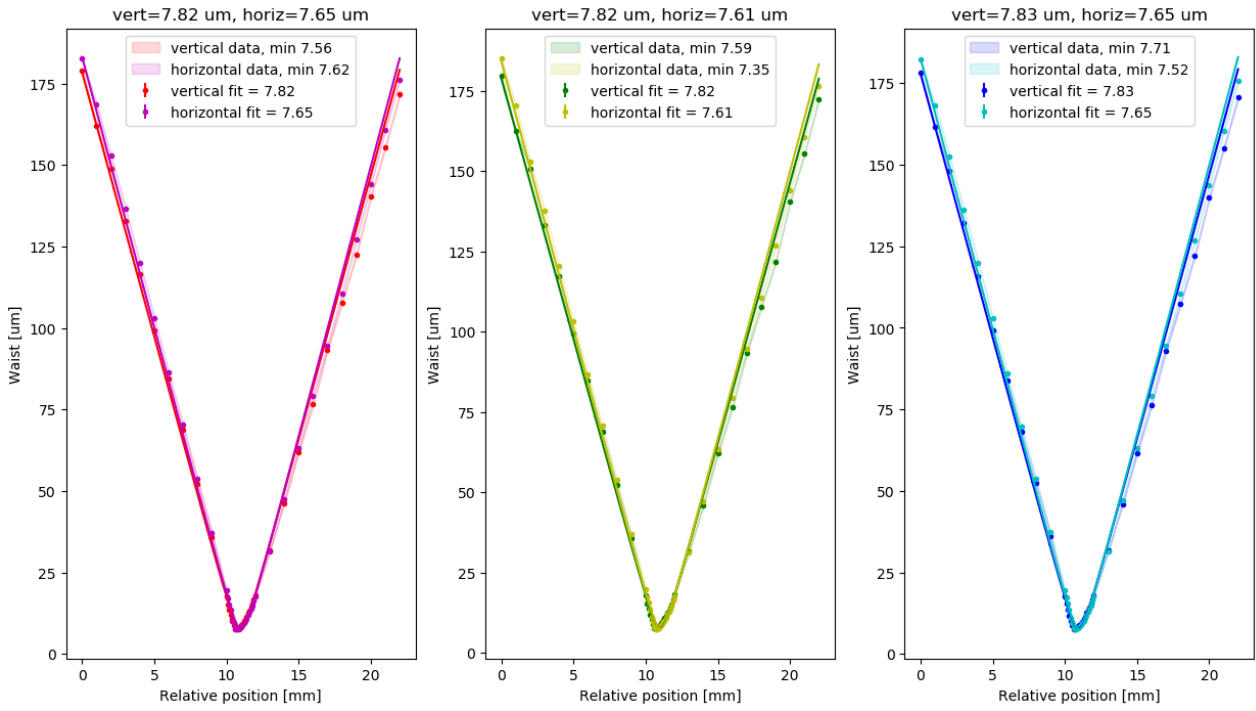
(a) PiCam.
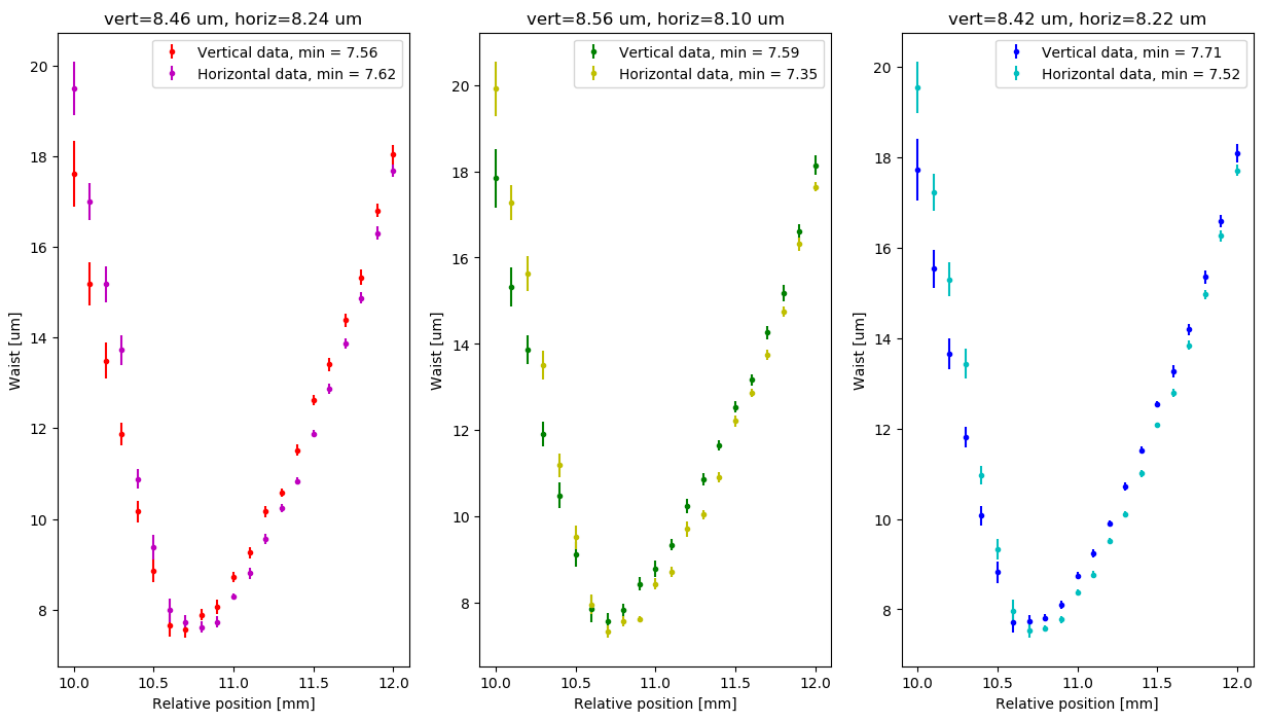
(b) PiCamZoom

Figure 41: RaspBerryCam.

Looking at the images of the blue pixels on figure 42, it is seen that the beam seems to have a dark spot just before the focus. This spot is neither visible at the start position, nor after the spot.

Figure 42: Images of the spot at different positions.
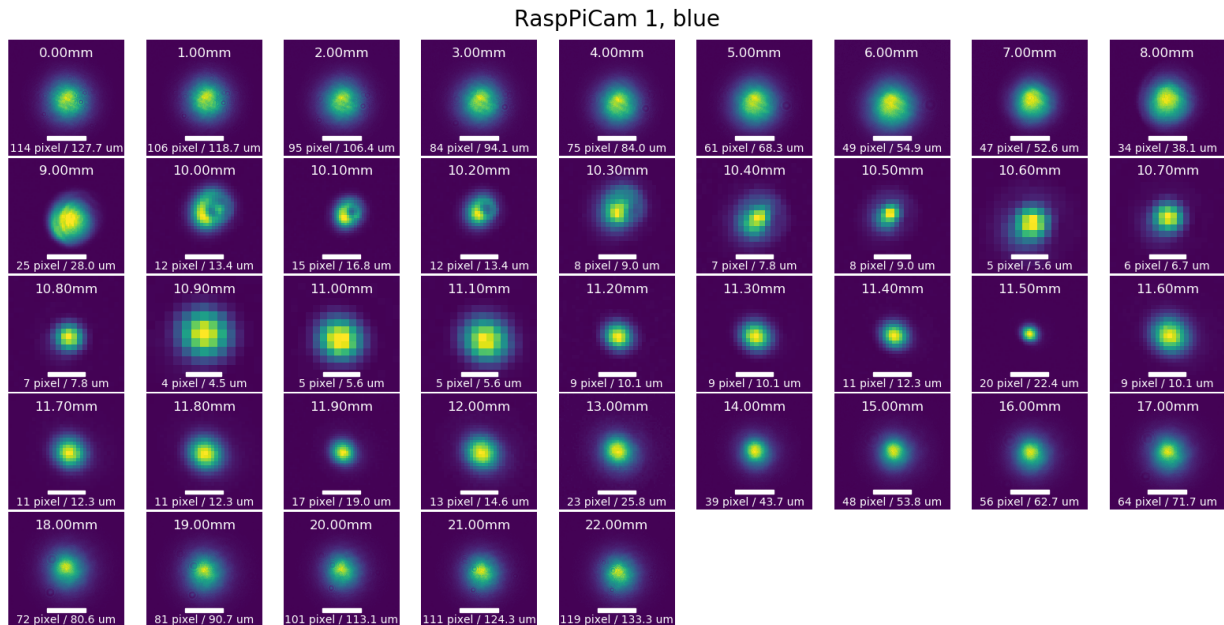
4.2.3   Summary

The Raspberry Pi camera confirms that the focus of the spot size have the correct size of around 7.6 µm, as was previously established with the Lumenera camera. However the beam was focusing sharper than it is diverging, and exhibited a dark spot in the beam just before the focus. This points toward that it is the beam itself that is not behaving nicely.

4.3 Polarization Issues

At the nearing of the end of this thesis, it was realized that there was some fundamental problems with nearly all polarization optics bought for, some of it already used in, the experiment. The issues encountered and describe in this thesis were some of the first indications that the polarization optics were not behaving nicely. This suspicion was further reinforced, when writing with other ytterbium groups around the world, whom confirmed that issues with near ultra-violet light and optics were a problem. The problem especially seems to arise from the optical cement used, for example in zero-order waveplates and beam splitter. However none of the groups asked had had any issues with cemented doublets.

To see if the 50/50 beam splitter used in the setup for polarization stability, as seen on figure 16, a test was made. By placing two photodiodes to detect the reflected and the transmitted signal, it was seen that when rotating a HWP infront of the 50/50 BS the relfected and transmitted signal where changing. This can be seen on figure 43.
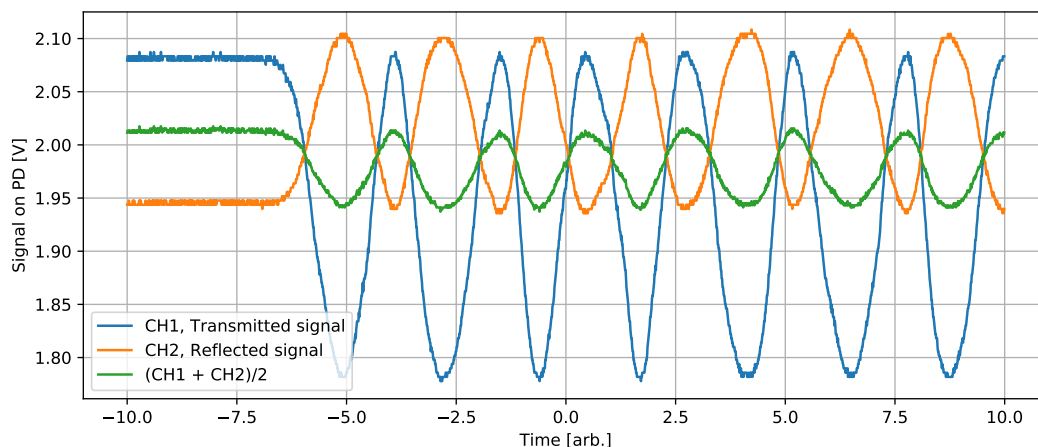

Figure 43: 50/50 beam splitter test.

Evidently, the 50/50 BS is also dependent on the polarization, further casting doubt that any meaningful conclusion regarding the polarization stability of the photonic crystal fiber is possible with the presented measurements in chapter 3.2.

This could very well explain poor polarization stability of the PCF. As both in the linear polarization for beam incoupling with the zero-order half-wave plate and the two cubes after the fiber, would introduce many unknowns, making it impossible to say if the PCF or the optics is to blame for the polarization fluctuation observed.

Furthermore, by looking closely at the optical cement of a PBS with a high power beam going through, it was seen that the cement would start to glow with a greenish color, which were strange considering that the wavelength of the light was near UV at around 399 nm.
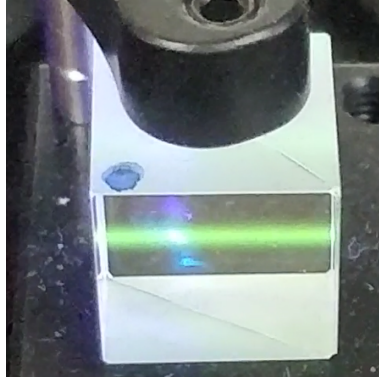
Figure 44: Glowing optical cement.

Some damage was also seen on a cemented HWP, used in front of the Rydberg laser. There was a distinct burned mark of the waveplate, which had not been seen on any of the more used MO-HWP, which are not cemented.

The inconclusive results from the probe spot size measurements, should not be directly affected by the issues with the polarization optics, but as the current plan is to used cemented achromats, it will have to be further investigated if the lenses or the imaging that is causing problems.

5 Conclusion and Outlook

5.1 Conclusion

In the scope of this thesis the probe and control laser setup for a new, ultracold ytterbium experiment for nonlinear quantum optics based on Rydberg atoms was partly designed and characterized. The status of the probe and control setup is however put on hold for now, as a big issue with the polarization optics were discovered at the end of this thesis. Due to time constrains a more thorough investigating into the polarization issues could not be taken.

As all measurement in some form or another have been relying on polarization optics, no trustworthy results have been obtained. However a thorough motivation for use of ytterbium were given in chapter 1. In chapter 2 a summary of the design decisions were lay out.

5.2 Outlook

The first step for the new ytterbium experiment was taken at the start of 2018. The new laboratory was ready to be moved into half a year later. Setting up the laser table and further refining the design of the finale experiment was done in the second half of 2018, and at the start of 2019 the first pieces of the final experimental chamber was put together.

At submission data, the experiment whole experiment both the 2D MOT chamber and the science chamber is constructed and under ultra-high vacuum. The first ytterbium in the 2D MOT chamber have been seen, but because of unexpected issues, partly the bad polarization optics discussed in this thesis, partly some other unrelated optics problems, the 2D MOT is still not working as designed. New polarization optics for the whole experiment have been ordered, and it is the plan that before the end of 2019, that the first ytterbium atoms will be trapped in the 2D MOT and transferred to a functioning 3D MOT.
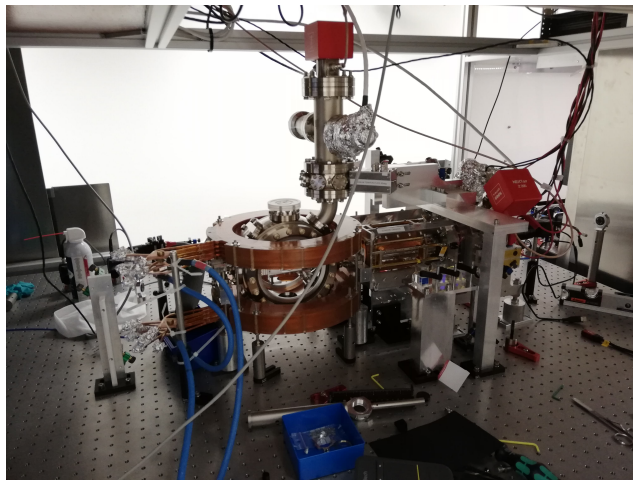
Figure 45: First ytterbium seen in 2D MOT chamber.

References

[1] P. Bienias et al. "Scattering resonances and bound states for strongly interacting Rydberg polaritons". In: *Phys. Rev. A* 90 (5 Nov. 2014), p. 053804. DOI: `10.1103/PhysRevA.90.053804`.

[2] Johannes Otterbach et al. "Wigner Crystallization of Single Photons in Cold Rydberg Ensembles". In: *Phys. Rev. Lett.* 111 (11 Sept. 2013), p. 113001. DOI: `10.1103/PhysRevLett.111.113001`.

[3] Matthias Moos et al. "Many-body physics of Rydberg dark-state polaritons in the strongly interacting regime". In: *Phys. Rev. A* 92 (5 Nov. 2015), p. 053846. DOI: `10.1103/PhysRevA.92.053846`. URL: `https://link.aps.org/doi/10.1103/PhysRevA.92.053846`.

[4] Ofer Firstenberg et al. "Attractive photons in a quantum nonlinear medium". In: *Nature* 502 (Sept. 2013). DOI: `10.1038/nature12512`.

[5] Richard P. Feynman. "Simulating physics with computers". In: *International Journal of Theoretical Physics* 21.6 (June 1982), pp. 467–488. ISSN: 1572-9575. DOI: `10.1007/BF02650179`.

[6] Michael A. Nielsen and Isaac L. Chuang. *Quantum Computation and Quantum Information: 10th Anniversary Edition*. Cambridge University Press, 2010. DOI: `10.1017/CBO9780511976667`.

[7] H John Caulfield and Shlomi Dolev. "Why future supercomputing requires optics". In: *Nat. Photonics* 4 (May 2010). DOI: `10.1038/nphoton.2010.94`.

[8] P. A. Franken et al. "Generation of Optical Harmonics". In: *Phys. Rev. Lett.* 7 (4 Aug. 1961), pp. 118–119. DOI: `10.1103/PhysRevLett.7.118`.

[9] Tatjana Wilk et al. "Single-Atom Single-Photon Quantum Interface". In: *Science* 317.5837 (2007), pp. 488–490. ISSN: 0036-8075. DOI: `10.1126/science.1143835`. eprint: `http://science.sciencemag.org/content/317/5837/488.full.pdf`.

[10] Danny O'Shea et al. "Fiber-Optical Switch Controlled by a Single Atom". In: *Phys. Rev. Lett.* 111 (19 Nov. 2013), p. 193601. DOI: `10.1103/PhysRevLett.111.193601`.

[11] Thomas F. Gallagher. *Rydberg Atoms*. Cambridge Monographs on Atomic, Molecular and Chemical Physics. Cambridge University Press, 1994. DOI: `10.1017/CBO9780511524530`.

[12] M. Saffman, T. G. Walker, and K. Mølmer. "Quantum information with Rydberg atoms". In: *Rev. Mod. Phys.* 82 (3 Aug. 2010), pp. 2313–2363. DOI: `10.1103/RevModPhys.82.2313`.

[13]   Inbal Friedler et al. "Long-range interactions and entanglement of slow single-photon pulses". In: *Phys. Rev. A* 72 (4 Oct. 2005), p. 043803. DOI: 10.1103/PhysRevA.72.043803.

[14]   Sebastian Weber et al. "Calculation of Rydberg interaction potentials". In: *Journal of Physics B: Atomic, Molecular and Optical Physics* 50.13 (2017), p. 133001.

[15]   M. D. Lukin et al. "Dipole Blockade and Quantum Information Processing in Mesoscopic Atomic Ensembles". In: *Phys. Rev. Lett.* 87 (3 June 2001), p. 037901. DOI: 10.1103/PhysRevLett.87.037901.

[16]   Y. O. Dudin and A. Kuzmich. "Strongly Interacting Rydberg Excitations of a Cold Atomic Gas". In: *Science* 336.6083 (2012), pp. 887–889. ISSN: 0036-8075. DOI: 10.1126/science.1217901. eprint: http://science.sciencemag.org/content/336/6083/887.full.pdf.

[17]   Asaf Paris-Mandoki et al. "Free-Space Quantum Electrodynamics with a Single Rydberg Superatom". In: *Phys. Rev. X* 7 (4 Oct. 2017), p. 041010. DOI: 10.1103/PhysRevX.7.041010.

[18]   Michael Fleischhauer, Atac Imamoglu, and Jonathan P. Marangos. "Electromagnetically induced transparency: Optics in coherent media". In: *Rev. Mod. Phys.* 77 (2 July 2005), pp. 633–673. DOI: 10.1103/RevModPhys.77.633.

[19]   M. Fleischhauer and M. D. Lukin. "Dark-State Polaritons in Electromagnetically Induced Transparency". In: *Phys. Rev. Lett.* 84 (22 May 2000), pp. 5094–5097. DOI: 10.1103/PhysRevLett.84.5094.

[20]   Lene Vestergaard Hau et al. "Light speed reduction to 17 m per second in an ultracold atomic gas. Nature 397, 594-598". In: *Nature* 397 (Feb. 1999). DOI: 10.1038/17561.

[21]   J. D. Pritchard et al. "Cooperative Atom-Light Interaction in a Blockaded Rydberg Ensemble". In: *Phys. Rev. Lett.* 105 (19 Nov. 2010), p. 193603. DOI: 10.1103/PhysRevLett.105.193603.

[22]   Alexey V. Gorshkov et al. "Photon-Photon Interactions via Rydberg Blockade". In: *Phys. Rev. Lett.* 107 (13 Sept. 2011), p. 133602. DOI: 10.1103/PhysRevLett.107.133602.

[23]   M. J. Gullans et al. "Effective Field Theory for Rydberg Polaritons". In: *Phys. Rev. Lett.* 117 (11 Sept. 2016), p. 113601. DOI: 10.1103/PhysRevLett.117.113601.

[24]   Krzysztof Jachymski, Przemysław Bienias, and Hans Peter Büchler. "Three-Body Interaction of Rydberg Slow-Light Polaritons". In: *Phys. Rev. Lett.* 117 (5 July 2016), p. 053601. DOI: 10.1103/PhysRevLett.117.053601.

[25]   C. Gaul et al. "Resonant Rydberg Dressing of Alkaline-Earth Atoms via Electromagnetically Induced Transparency". In: *Phys. Rev. Lett.* 116 (24 June 2016), p. 243001. DOI: 10.1103/PhysRevLett.116.243001.

[26]   F B Dunning et al. "Recent advances in Rydberg physics using alkaline-earth atoms". In: *Journal of Physics B: Atomic, Molecular and Optical Physics* 49 (June 2016), p. 112003. DOI: 10.1088/0953-4075/49/11/112003.

[27]   J. Millen, G. Lochead, and M. P. A. Jones. "Two-Electron Excitation of an Interacting Cold Rydberg Gas". In: *Phys. Rev. Lett.* 105 (21 Nov. 2010), p. 213004. DOI: 10.1103/PhysRevLett.105.213004.

[28]   D. P. Sadler et al. "Radiation trapping in a dense cold Rydberg gas". In: *Phys. Rev. A* 95 (1 Jan. 2017), p. 013839. DOI: 10.1103/PhysRevA.95.013839.

[29]   Ryan K Hanley et al. "Probing interactions of thermal Sr Rydberg atoms using simultaneous optical and ion detection". In: *Journal of Physics B: Atomic, Molecular and Optical Physics* 50.11 (2017), p. 115002. URL: http://stacks.iop.org/0953-4075/50/i=11/a=115002.

[30]   Santosh Pisharody. "Electron Dynamics in double Rydberg Wavepackets". PhD Thesis. Technical Institute of Technology, Bombay, 2003.

[31]   S. N. Pisharody and R. R. Jones. "Probing Two-Electron Dynamics of an Atom". In: *Science* 303.5659 (2004), pp. 813–815. ISSN: 0036-8075. DOI: 10.1126/science.1092220. URL: http://science.sciencemag.org/content/303/5659/813.

[32]   R Mukherjee et al. "Many-body physics with alkaline-earth Rydberg lattices". In: *Journal of Physics B: Atomic, Molecular and Optical Physics* 44.18 (2011), p. 184010. URL: http://stacks.iop.org/0953-4075/44/i=18/a=184010.

[33]   Darrick E. Chang, Vladan Vuletić, and Mikhail D. Lukin. "Quantum nonlinear optics — photon by photon". In: *Nature Photonics* 8.9 (Sept. 2014), pp. 685–694. ISSN: 1749-4885. DOI: 10.1038/nphoton.2014.192. URL: http://www.nature.com/articles/nphoton.2014.192.

[34]   Bastian Hacker et al. "A photon–photon quantum gate based on a single atom in an optical resonator". In: *Nature* 536.7615 (Aug. 2016), pp. 193–196. ISSN: 0028-0836. DOI: 10.1038/nature18592. URL: http://www.nature.com/articles/nature18592.

[35]   Andreas Reiserer and Gerhard Rempe. "Cavity-based quantum networks with single atoms and optical photons". In: *Reviews of Modern Physics* 87.4 (Dec. 2015), pp. 1379–1418. ISSN: 0034-6861. DOI: 10.1103/RevModPhys.87.1379. URL: https://link.aps.org/doi/10.1103/RevModPhys.87.1379.

[36]   O Firstenberg, C S Adams, and S Hofferberth. "Nonlinear quantum optics mediated by Rydberg interactions". In: *Journal of Physics B: Atomic, Molecular and Optical Physics* 49.15 (Aug. 2016), p. 152003. ISSN: 0953-4075. DOI: 10.1088/0953-4075/49/15/152003. URL: http://stacks.iop.org/0953-4075/49/i=15/a=152003?key=crossref.c5970f07d580ff994fcb28d3ed09f4e3.

[37]   Thomas F. Gallagher and Cambridge University Press. *Rydberg Atoms*. Cambridge University Press, 1994, p. 512. ISBN: 9780511524530.

[38]   M. D. Lukin et al. "Dipole Blockade and Quantum Information Processing in Mesoscopic Atomic Ensembles". In: *Physical Review Letters* 87.3 (June 2001), p. 037901. ISSN: 0031-9007. DOI: 10.1103/PhysRevLett.87.037901. URL: https://link.aps.org/doi/10.1103/PhysRevLett.87.037901.

[39]   Nina Stiesdal. "Intrinsic three photon correlations mediated by a single Rydberg super-atom". Master Thesis. University of Southern Denmark, 2018.

[40]   Hannes Busche, Simon W. Ball, and Paul Huillery. "A high repetition rate experimental setup for quantum non-linear optics with cold Rydberg atoms". In: *The European Physical Journal Special Topics* 225.15 (Dec. 2016), pp. 2839–2861.

[41]   Thibault Peyronel et al. "Quantum nonlinear optics with single photons enabled by strongly interacting atoms". In: *Nature* (2012). ISSN: 00280836. DOI: 10.1038/nature11361.

[42]   Ofer Firstenberg et al. "Attractive photons in a quantum nonlinear medium". In: *Nature* 502.7469 (Oct. 2013), pp. 71–75. URL: http://proxy1-bib.sdu.dk:2048/login?url=https://search-proquest-com.proxy1-bib.sdu.dk/docview/1445365562?accountid=14211.

[43]   Asaf Paris-Mandoki et al. "Free-Space Quantum Electrodynamics with a Single Rydberg Superatom". In: *Phys. Rev. X* 7 (4 Oct. 2017), p. 041010. DOI: 10.1103/PhysRevX.7.041010. URL: https://link.aps.org/doi/10.1103/PhysRevX.7.041010.

[44]   Y O Dudin et al. "Observation of coherent many-body Rabi oscillations". In: *Nature Physics* 8 (2012). DOI: 10.1038/NPHYS2413. URL: https://search-proquest-com.proxy1-bib.sdu.dk/docview/1144278840?pq-origsite=summon.

[45]   T. G. Tiecke et al. "Nanophotonic quantum phase switch with a single atom". In: *Nature* 508.7495 (Apr. 2014), pp. 241–244. ISSN: 0028-0836. DOI: 10.1038/nature13188. URL: http://www.nature.com/doifinder/10.1038/nature13188.

[46]   H. Gorniaczyk et al. "Single-Photon Transistor Mediated by Interstate Rydberg Inter-actions". In: *Physical Review Letters* 113.5 (July 2014), p. 053601. ISSN: 0031-9007. DOI: 10.1103/PhysRevLett.113.053601. URL: https://link.aps.org/doi/10.1103/PhysRevLett.113.053601.

[47] E. Urban et al. "Observation of Rydberg blockade between two atoms". In: *Nature Physics* 5.2 (2009), p. 110.

[48] C. Tresp et al. "Single-Photon Absorber Based on Strongly Interacting Rydberg Atoms". In: *Phys. Rev. Lett.* 117 (22 Nov. 2016), p. 223001. DOI: 10.1103/PhysRevLett.117. 223001. URL: https://link.aps.org/doi/10.1103/PhysRevLett.117.223001.

[49] Y. Takasu et al. "High-Density Trapping of Cold Ytterbium Atoms by an Optical Dipole Force". In: *Phys. Rev. Lett.* 90 (2 Jan. 2003), p. 023003. DOI: 10.1103/PhysRevLett. 90.023003.

[50] Takeshi Fukuhara et al. "Degenerate Fermi Gases of Ytterbium". In: *Phys. Rev. Lett.* 98 (3 Jan. 2007), p. 030401. DOI: 10.1103/PhysRevLett.98.030401.

[51] L Franchi et al. "State-dependent interactions in ultracold 174 Yb probed by optical clock spectroscopy". In: *New Journal of Physics* 19.10 (2017), p. 103037.

[52] Francesco Scazza. "Probing SU(N)-symmetric orbital interactions with ytterbium Fermi gases in optical lattices". PhD Thesis. Munich University, 2015.

[53] Takuya Kohno et al. "One-Dimensional Optical Lattice Clock with a Fermionic 171 Yb Isotope". In: *Applied Physics Express* 2.7 (2009), p. 072501.

[54] Koen Sponselee et al. "Dynamics of Ultracold Quantum Gases in the Dissipative Fermi-Hubbard Model". In: *arXiv* (May 2018). DOI: arXiv:1805.11853.

[55] Alexey Gorshkov et al. "Two-orbital SU(N) magnetism with ultracold alkaline-earth atoms". In: *Nature Physics* 6 (Feb. 2010), p. 289. DOI: 10.1038/NPHYS1535.

[56] Y. Wang et al. "Dark State Optical Lattice with a Subwavelength Spatial Structure". In: *Phys. Rev. Lett.* 120 (8 Feb. 2018), p. 083601. DOI: 10.1103/PhysRevLett.120.083601.

[57] Shintaro Taie et al. "An SU(N) Mott insulator of an atomic Fermi gas realized by large-spin Pomeranchuk cooling". In: *Nature Physics* 8 (Aug. 2012). DOI: 10.1038/nphys2430.

[58] William McGrew et al. "Atomic clock performance enabling geodesy below the centime-tre level". In: *Nature* 564 (Nov. 2018). DOI: 10.1038/s41586-018-0738-2.

[59] Jacopo Grotti et al. "Geodesy and metrology with a transportable optical clock". In: *Nature Physics* 14 (May 2017). DOI: 10.1038/s41567-017-0042-3.

[60] C L Vaillant, M P A Jones, and R M Potvliege. "Long-range Rydberg–Rydberg interactions in calcium, strontium and ytterbium". In: *Journal of Physics B: Atomic, Molecular and Optical Physics* 45.13 (2012), p. 135004. URL: http://stacks.iop.org/0953-4075/45/i=13/a=135004.

[61] Ryuta Yamamoto et al. "An ytterbium quantum gas microscope with narrow-line laser cooling". In: *New Journal of Physics* 18.2 (2016), p. 023016. URL: http://stacks.iop.org/1367-2630/18/i=2/a=023016.

[62] Emanuele Distante et al. "Storing single photons emitted by a quantum memory on a highly excited Rydberg state". In: *Nature Communications* 8 (Jan. 2017), p. 14072. DOI: 10.1038/ncomms14072.

[63] Michael Berglund and Michael Wieser. "Isotopic compostions of the elements 2009 (IU-PAC technical report)". In: *Pure and Applied Chemistry* 83.2 (2011), pp. 48, 49. DOI: 10.1351/PAC-REP-10-06-02.

[64] G. Audi, A.H. Wapstra, and C. Thibault. "The AME2003 atomic mass evaluation - (II). Tables, graphs and references". working paper or preprint. Dec. 2003. URL: http://hal.in2p3.fr/in2p3-00014186.

[65] A.F. Hollemann. *Lehrbuch der anorganischen Chemie*. Walter de Gruyter, 1995.

[66] Sören Dörscher. "Creation of ytterbium quantum gases with a compact 2D-/3D-MOT setup". PhD Thesis. Universität Hamburg, 2013.

[67] Reina Maruyama. "Optical trapping of ytterbium atoms". PhD Thesis. Washington University, 2003.

[68] C. J. Foot. *Atomic Physics*. Great Clarendon Street, Oxford OX2 6DP: Oxford Master Series in Physics, 2005.

[69] Jeongwon Lee et al. "Core-shell magneto-optical trap for alkaline-earth-metal-like atoms". In: *Phys. Rev. A* 91 (5 May 2015), p. 053405. DOI: 10.1103/PhysRevA.91.053405.

[70] Mukherjee Rick. "Strong interactions in alkaline-earth Rydberg ensembles". PhD Thesis. Universität Dresden, Max-Planck Institut für Physik komplexer Systeme, 2013.

[71] Massimo Inguscio and Leonardo Fallani. *Atomic Physics - Precise Measurements and Ultracold Matter*. Great Clarendon Street - Oxford - OX2 6DP, United Kingdom: Oxford University Press, 2015, 155 ff.

[72] Malvin Teich Bahaa Saleh. *Fundamentals of Photonics*. New York, USA: Wiley-Interscience publication, 1991.

[73] Julia Emily Bjørnstrøm. "Advanced Optics for the Superfluid Flow of Atomic Quantum Mixtures". Master Thesis. University of Southern Denmark, August, 2018.

[74] Philipp Lunt. "Design and construction of a new ultracold ytterbium experiment for Rydberg physics". Master Thesis. University of Southern Denmark, 2019.

[75] Roger Ding. "Narrow Line Cooling of 84Sr". Master Thesis. Rice University, May, 2016.

[76] Markus Greiner et al. "Magnetic transport of trapped cold atoms over a large distance". In: *Phys. Rev. A* 63 (3 Feb. 2001), p. 031401. DOI: 10.1103/PhysRevA.63.031401.

[77] T. Kuwamoto et al. "Magneto-optical trapping of Yb atoms using an intercombination transition". In: *Phys. Rev. A* 60 (2 Aug. 1999), R745–R748. DOI: 10.1103/PhysRevA.60.R745. URL: https://link.aps.org/doi/10.1103/PhysRevA.60.R745.

[78] T. G. Tiecke et al. "High-flux two-dimensional magneto-optical-trap source for cold lithium atoms". In: *Phys. Rev. A* 80 (1 July 2009), p. 013409. DOI: 10.1103/PhysRevA.80.013409.

[79] Sören Dörscher et al. "Creation of quantum-degenerate gases of ytterbium in a compact 2D-/3D-magneto-optical trap setup". In: *Review of Scientific Instruments* 84.4 (2013), p. 043109. DOI: 10.1063/1.4802682.

[80] Jürgen Appel, Andrew MacRae, and A I Lvovsky. "A versatile digital GHz phase lock for external cavity diode lasers". In: *Measurement Science and Technology* 20.5 (2009), p. 055302. URL: http://stacks.iop.org/0957-0233/20/i=5/a=055302.

[81] Hannes M. Gorniaczyk. "Single Photon Transistor mediated by electrically tunable Rydberg-Rydberg Interactions". PhD thesis. Universität Stuttgart, 2016.

[82] CC BY-SA 3.0 LaserSoft Imaging - Own work. *SilverFast USAF 1951 Resolution Target.* •. URL: https://commons.wikimedia.org/w/index.php?curid=12126324.

[83] CC BY-SA 3.0 By en:User:Cburnett. *Bayer pattern on sensor.* 2006. URL: https://commons.wikimedia.org/w/index.php?curid=1496872.

Acknowledgement

I could not have done this work alone. I would like to thank all persons who contributed directly or indirectly to my work. Especially a deep thanks to

- My supervisor *Sebastian Hofferberth*, for giving me the opportunity of working on the new experiment with this amazing group. I will look forward to hear about the progression of the experiment, and hopefully some day soon, probe the first ytterbium in the 3D MOT.

- All group member, both current; *Nina Stiesdal, Stuti Gugnani, Hannes Busche, Mohammad Noaman,* and former; *Simon Ball, Philipp Lunt, Julia Bjørnstrøm.* It have been a pleasure working with all of you. I would probably have gotten a ryebread poisoning if not for us cooking together every day.

- *Nina Stiesdal*, for being the most optimistic and friendly person. You almost supernatural ability of being (almost) always happy and helpful. Many thanks for helping me with feedback on this thesis, and for increasing my, at times lacklustre, motivation. And for having you to back me up, when trying to convince the rest of the group of weird Danish traditions.

- *Mohammad Noaman*, for always being up for discussing, whether it be about global politics, Indian movies or physics. A big thank you for proof reading this thesis and giving me feed back. Crossing my fingers that you will spend the next many years in Denmark.

- *Stuti Gugnani*, for always being super friendly, and bringing in even more variety to our daily cooking. Also a big thank you for being the person, to whom I can tell the exact same thing to, as I was told when I first started; "if the fibercoupling are not behaving, then keep doing it".

- *Hannes Busche*, for always being available with the expert knowledge that comes with old age and being happy to share it. And for making great food by using *all* available pots and pans in the kitchen.

- *Simon Ball*, for helping me learn the ropes when I started in the lab, and for his dry humour and giving a somewhat depressing insight into British politics.

- *Philipp Lunt*, for resisting all attempts of learning to speak proper Danish. But I still have hope for you to someday being able to order *rugbrød* on fluently. Also thanks for all the cooperation in the lab, and always having *something* to put on Spotify.